Monthly Notices of the ROYAL ASTRONOMICAL SOCIETY

MNRAS **513,** 311–332 (2022) https://doi.org/10.1093/mnras/stac198
Advance Access publication 2022 January 28

Globally optimal shape and spin pole determination with light-curve inversion

Chee-Kheng Chng [1,2]★ Michele Sasdelli[1,2] and Tat-Jun Chin[1,2]

[1]*Australian Institute for Machine Learning, Corner Frome Road and, North Terrace, Adelaide SA 5000, Australia*
[2]*School of Computer Science, University of Adelaide, Adelaide SA 5000, Australia*

Accepted 2022 January 17. Received 2022 January 15; in original form 2021 July 18

ABSTRACT

Light-curve inversion is an established technique in determining the shape and spin states of an asteroid. However, the front part of the processing pipeline, which recovers the spin pole and area of each facet, is a non-convex optimization problem. Hence, any local iterative optimization scheme can only promise a locally optimal solution. Apart from the obvious downsides of getting a non-optimal solution and the need for an initialization scheme, another major implication is that it creates an ambiguous scenario – which is to be blamed for the remaining residual? The inaccuracy of the modelling, the integrity of the data, or the non-global algorithm? We address the last uncertainty in this paper by embedding the spin pole and area vector determination module in a deterministic global optimization framework. To the best of our knowledge, this is the first attempt to solve these parameters globally. Specifically, given calibrated light-curve data, a scattering model for the object, and spin period, our method outputs the globally optimal spin pole and area vector solutions. One theoretical contribution of this paper is the introduction of a lower bound error function that is derived based on (1) the geometric relationship between the incident and scattered light on a surface and (2) the uncertainty of the gap between the observed and estimated brightness at a particular epoch in a light curve. We validated our method's ability in achieving global minimum with both simulated and real light-curve data. We also tested our method on the real light curves of four asteroids.

Key words: methods: numerical – minor planets, asteroids: general.

1 INTRODUCTION

Light curve is a set of time-series brightness data. Such measurement is usually collected from a consistent source to study its properties. The variation in the light curve is mainly caused by the shape and spinning motion of the object. If a light scattering law is assumed, one can also deduce the scattering property of the surface.

The intensity measurement at each epoch of the light curve is essentially the disc-integrated brightness of the observed surface. Russell (1906) laid down the mathematical foundation of such integration; and concluded that it is not possible to determine the shape of the asteroid with only light curves observed at opposition geometry.[1] A century later, Kaasalainen et al. (1992a), Kaasalainen, Lamberg & Lumme (1992b) show that by including light curves at non-zero phase angle geometries and a light scattering law in the modelling, there are methods in obtaining a shape solution. A decade after that, a robust light-curve inversion tool was presented by Kaasalainen & Torppa (2001), Kaasalainen, Torppa & Muinonen (2001), which is one of the standard tools in today's asteroid studies. Even though the tool is commonly associated with asteroids, it can also be applied to other atmosphere-less bodies (see Kaasalainen et al. 1992a). As such, we use the term 'object' instead of 'asteroid' in our paper for the sake of generality.

Apart from the robustness of the tool, another crucial factor that motivates its popularity is the accessibility of light curve. In principle, it is available for all Resident Space Object (RSO) with a ground-based sensor. Recently, several works (see Friedman & Frueh 2018; Fan, Friedman & Frueh 2019; Fan & Frueh 2020) started to explore its potential outside of the asteroid realm, building on top of the mentioned light-curve inversion tool to reconstruct the shape of artificial space objects.

The method put forward by Kaasalainen & Torppa (2001) [the KTM (Authors' initial) method hereafter] has seen wide applications in the asteroid research community, see for instance Ďurech, Hanuš & Ali-Lagoa (2018), Ďurech et al. (2011), Hanuš, Marchis & Ďurech (2013), Hanuš et al. (2011), Vokrouhlickỳ et al. (2017a), Pravec et al. (2019), Vokrouhlickỳ et al. (2017b), Rożek et al. (2019), Monteiro et al. (2020), Tanga et al. (2015). As of 2021 July, there are 5715 models, each with unique convex shapes and spin states recovered with KTM's method from 3303 asteroids' light curves. These models are currently available in the Database of Asteroid Models from Inversion Techniques (DAMIT) Ďurech, Sidorin & Kaasalainen (2010). It is also sometimes referred to as the convex light-curve inversion tool since the convex shape assumption variant is the most popular one due to its stability.

Several attempts were made to extend KTM's method. Viikinkoski, Kaasalainen & Ďurech (2015) introduced ADAM, which combines the disc-resolved data (adaptive optics or other images,

★ E-mail: cheekheng.chng@adelaide.edu.au

[1]Also known as the zero phase angle geometry, where the observing and illumination directions are parallel to each other.

interferometry, and range-Doppler radar data) and the disc-integrated data (light curves) to reconstruct asteroid shape models. The additional disc-resolved data helps in further constraining the shape of the model. Meanwhile, Ďurech et al. (2011) incorporated occultation silhouettes to the convex models reconstructed by KTM's method to determine the absolute size of the asteroids.

The inversion quality of KTM's method relies heavily on the quality of the light curves – it should be fairly dense, covering the entire spin period, and observed at diverse Sun-asteroid-observer geometries. In an attempt to exploit the sparse light-curve data (e.g. the data collected during the *Gaia* mission), Carbognani et al. (2012) investigated a simpler shape representation for the asteroid (which has fewer parameters) in the inversion process. Their investigation on several asteroids reveals that the spin poles and periods recovered with a tri-axial ellipsoid generally agree with KTM's solutions with a complex shape. Muinonen & Lumme (2015) further pushed the ellipsoidal asteroid model by integrating the Lommel-Seeliger surface reflection model. Along the same line of work, Muinonen et al. (2015) incorporated the Markov-chain Monte Carlo (MCMC) analysis to describe the probability density function in the neighbourhood regions of the best-fitting parameters.

The aforementioned ellipsoidal model methods trade speed with accuracy. Wang et al. (2015) pointed out that the spin pole determination from these methods is unreliable when the asteroid diverges from the ellipsoidal shape. Hence, Wang et al. (2015) implemented a similar MCMC analysis on KTM's method to obtain an uncertainty assessment for the spin pole and period estimation. Recently, Muinonen et al. (2020) introduced a novel proposal probability density function for their MCMC sampler. Their experiments show that the proposed statistical inversion method provides realistic uncertainty estimations.

Bartczak & Dudziński (2018) introduced an algorithm that relaxes the usual convex-shaped assumption in the light-curve inversion process. The proposed method, named SAGE, is developed based on the genetic algorithm. In essence, SAGE generates and evaluates random shapes and spin-axis mutations in each iteration until a stable solution is found. Bartczak & Dudziński (2019) later proposed a novel assessment method for asteroid models based on sensitivity analysis. The proposed scheme first generates a large number of clones given an asteroid model reconstructed by any light-curve inversion method. Then, the clones that produce similar light curves (within an error threshold) are retained. Lastly, the largest and smallest asteroids in the family of clones are used to assign a volume uncertainty to the assessed model.

Lumme, Karttunen & Bowell (1990)'s work is one of the earliest methods to estimate the spin pole orientation from zero-phase-angle light curves. Underpinning Lumme et al. (1990)'s work is the expression of light curves with the spherical harmonics expansion. By assuming a tri-axial ellipsoid model, the algorithm searches for the spin pole parameters expressed in the truncated series with a non-linear least-squares optimization scheme. The pioneering work shows that despite the truncation and light-curve extrapolation (to get zero-phase-angle light curves), its spin pole estimate is only about 5° off from the real spin pole in their synthetic light-curve experiments.

Recently there has been a growing trend in casting the shape estimation task as a classification problem and solving it with deep learning approaches. Linares, Furfaro & Reddy (2020) trained a Convolutional Neural Network (CNN) to determine the type of space objects based on the light-curve data alone. Allworth et al. (2021) shown that transferring the knowledge learnt on simulated light-curve data helps us to improve the deep network's performance on the shape classification task with real light-curve data.

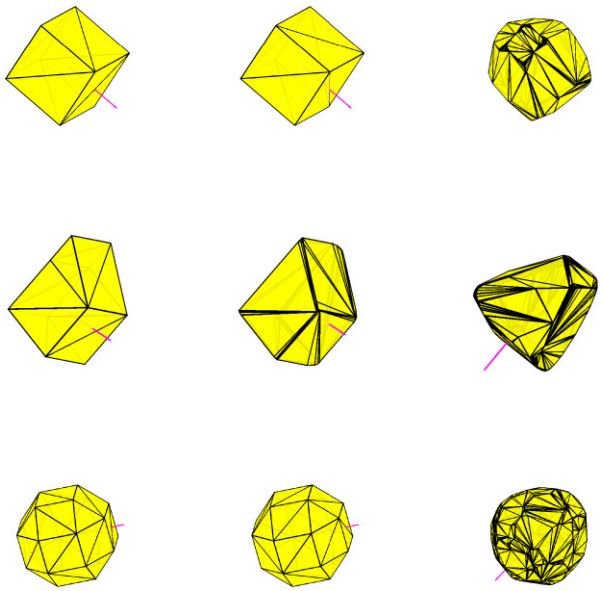

Figure 1. Left to right: Ground-truths, global solutions from our method, local solutions from KTM's method, pink arrows represent the spin poles. These sub-optimal solutions illustrate the local minima that KTM's method converged to when it is poorly initialized.

Assuming all other parameters of the object (e.g. spin period and scattering parameters) are known, the light-curve inversion problem with Kaasalainen & Torppa (2001)'s model is a bilinear (non-convex) problem in the domain of the spin pole and surface area of the object. Consequently, solving such a problem with any local optimization method is prone to suboptimal solutions. KTM's method is one of the examples. Fig. 1 illustrates some of the suboptimal solutions obtained with KTM's method given bad initialization. A systematic initialization scheme is a common remedy for a local method to increase the likelihood of obtaining a globally optimal solution. The procedural steps of running KTM's method as presented in Kaasalainen et al. (2001) is summarized in Algorithm 1. Two different steepest descent solvers (with different problem formulations) underpin KTM's method. The first one uses a straightforward representation where the area of each facet is expressed explicitly in the formulation, also known as the extended Gaussian image (EGI) representation (Horn 1984). It is solved using the conjugate gradient method (CG solver hereafter). The second one represents the surface's curvature function as a spherical harmonics series where the coefficients of the function series are the variables of interest. It has fewer parameters to be solved, and uses a Levenberg–Marquardt optimization strategy (LM solver hereafter). Both the mentioned optimization algorithms can be referred to in Press et al. (1996)'s work. In essence, the inversion tool is run multiple times with a set of spin pole initial estimates $\{\boldsymbol{\omega}_0\}_{k=1}^{K}$, and the model with the lowest fitting error is chosen as the solution. However, we highlight that an initialization scheme offers no guarantee in finding a globally optimal solution.

In this work, we introduce a guaranteed globally optimal algorithm for the spin pole and shape estimation. Specifically, our method jointly searches for the optimal combination of a spin pole and surface areas (of a densely sampled EGI) associated with the global minimum error of the light-curve model proposed by Kaasalainen & Torppa (2001) (see Section 2 for more details). The proposed algorithm is built upon the Branch-and-Bound framework (see Horst & Tuy 2013, chap. 4), one of the well-known deterministic global optimization methods. To the best of our knowledge, this is the first

Algorithm 1 Lightcurve inversion algorithm by Kaasalainen et al. (2001)

Require: $\boldsymbol{l} \in \mathbb{R}^I$, $\{\boldsymbol{\omega}_0\}_{k=1}^K$, $\mathbf{N} \in \mathbb{R}^{3\times J}$, P
1: **for** $k = 1,...,$ K **do**
2: $\quad \boldsymbol{\omega}_k^*, f_k^* \leftarrow$ spherical harmonics LM solver $(\boldsymbol{\omega}_{0k}, \boldsymbol{l}, \mathbf{N}, P)$
3: **end for**
4: $k^* = argmin(\{f_k^*\}_{k=1}^K)$
5: $\boldsymbol{g}^* \leftarrow$ polyhedra conjugate gradients solver $(\boldsymbol{\omega}_{k^*}^*, \boldsymbol{l}, \mathbf{N}, P)$
6: $\boldsymbol{h} \leftarrow$ Minkwoski minimization$(\boldsymbol{g}^*, \mathbf{N})$
7: $V, G \leftarrow$ convex hull determination$(\boldsymbol{g}^*, \boldsymbol{h}, \mathbf{N})$
8: **return** $\boldsymbol{\omega}_{k^*}^*, V, G$;

attempt to incorporate a global optimization scheme into the light-curve inversion problem.

The remaining of this paper is structured as follows: Section 2 lays down the formulations of the light-curve inversion problem, Section 3 details the design of our algorithm and the derivation of the bounding function; Section 4 presents the conducted experiments, and we conclude in Section 5.

2 PRELIMINARIES

As stated in Kaasalainen & Torppa (2001)'s work, the observed brightness l_i at each epoch t_i, can be expressed as a function of the areas of the illuminated and visible surfaces,

$$l_i = \boldsymbol{a}_i^\intercal \boldsymbol{g}\,, \tag{1}$$

where $\intercal$ represents the transpose operation, $\boldsymbol{g} \in \mathbb{R}^J$ is the area vector, and the vector $\boldsymbol{a}_i \in \mathbb{R}^J$ embeds the light scattering law and the orientation of the object at epoch t_i (see equation 14 for the full expression). The surface that is not visible and illuminated is nullified with $a_{ij} = 0$ since it does not contribute to the total observed brightness.

Hence, if $\boldsymbol{g}$ is the only unknown, the optimization problem can be written as follows,

$$\begin{aligned} \underset{\boldsymbol{g}}{min.} \quad & \left(\sum_{i=1}^{I}(\mid l_i - \boldsymbol{a}_i^\intercal \boldsymbol{g} \mid)^p\right)^{\frac{1}{p}} \\ \text{s.t.} \quad & \boldsymbol{g} \in \Omega, \end{aligned} \tag{2}$$

where p indicates the choice of norm. Note that the search of $\boldsymbol{g}$ is constrained within Ω,

$$\Omega = \{\boldsymbol{g} \in \mathbb{R}^J \mid \mathbf{N}\boldsymbol{g} = \boldsymbol{0}, \boldsymbol{g}_j \geq 0, j = 1, ..., J\}, \tag{3}$$

where the matrix $\mathbf{N} \in \mathbb{R}^{3\times J}$ packs in J surface normals of the object. These constraints are sufficient and necessary to ensure that the object is convex-shaped (see Kaasalainen et al. 1992a). It is clear from the linearity of the error function within the norm operation and the constraint functions that (2) is a convex optimization problem. Hence, the globally optimal $\boldsymbol{g}^*$ is guaranteed to be found with any local numerical solver (e.g. steepest descent method) since any local optimum is a global optimum in the problem of such nature (see Boyd, Boyd & Vandenberghe 2004).

Upon solving (2), we obtain the object's EGI, which is a set of surface normal vectors $\mathbf{N}$ and its corresponding area vector $\boldsymbol{g}$. Each convex polyhedron is defined uniquely by an EGI. Given an EGI, the final shape determination with Minkowski minimization is another convex optimization problem (see Little 1983). In other words, the (convex hull) shape reconstruction problem contains two sequential convex optimization problems, where the global optimal shape solution is guaranteed to be found.

However, if the spin pole of the object is unknown, the optimization problem degrades into a bilinear (non-convex) problem with the compact form below,

$$\begin{aligned} \underset{\boldsymbol{g},\boldsymbol{\omega}}{min.} \quad & \parallel \boldsymbol{l} - \mathbf{A}(\boldsymbol{\omega})\boldsymbol{g} \parallel_p \\ \text{s.t.} \quad & \boldsymbol{g} \in \Omega, \end{aligned} \tag{4}$$

where $\boldsymbol{\omega} = \{\lambda, \beta\}$ is the spin pole (λ and β represent the Euler angles of the spin pole). The reflectance of the surface is a function of its spin states [hence the notation $\mathbf{A}(\boldsymbol{\omega})$, see equations 14 to 17], alongside other parameters in the light scattering law. There are two different formulations to the convex shape inversion problem: (1) solving the facet areas of a triangulated polyhedral shape (4), and (2) the Gaussian surface density estimation via the spherical harmonics representation (see A1 in the supplementary material). Both formulations share the same bilinear property – the multiplication of the spin pole variables and the area vector or the coefficients of spherical harmonics.

In principle, there is no guaranteed way of obtaining a global optimal solution when solving a non-convex problem with a local optimization method. As such, we solve problem (4) with a global optimization method – Branch-and-Bound (BnB). As an overview, our proposed algorithm detaches the search for the spin pole and the area vector of EGI, which is formulated as follows:

$$\begin{aligned} \underset{\boldsymbol{\omega}\in\mathbb{S}}{min} \quad \underset{\boldsymbol{g}}{min.} \quad & \parallel \boldsymbol{l} - \mathbf{A}(\boldsymbol{\omega})\boldsymbol{g} \parallel_p, \\ \text{s.t.} \quad & \boldsymbol{g} \in \Omega, \end{aligned} \tag{5}$$

where $\mathbb{S}$ represents the domain of $\boldsymbol{\omega}$ (detailed in Section 3.3.2). The outer optimal $\boldsymbol{\omega}$ is searched with a BnB framework, while the inner problem is cast as a linear programming (LP) problem (see Nocedal & Wright 2006, chap. 13).

3 PROPOSED METHOD

Our proposed algorithm is summarized in Algorithm 2. We start by breaking down the formulation in (5). Then, the bedrock of our algorithm – the novel lower bound function, is presented. This section then proceeds with the reformulation to LP problems, implementation details, and ends with the observational uncertainty treatment.

3.1 Problem formulation

First, given the following objective function,

$$f(\boldsymbol{g} \mid \boldsymbol{\omega}) = \parallel \boldsymbol{l} - \mathbf{A}(\boldsymbol{\omega})\boldsymbol{g} \parallel_p, \tag{6}$$

the inner constrained optimization problem (denoted as P_0) solves for the globally optimal $\boldsymbol{g}$ given a particular $\boldsymbol{\omega}$,

$$\begin{aligned} P_0 : \underset{\boldsymbol{g}}{min.} \quad & f(\boldsymbol{g} \mid \boldsymbol{\omega}), \\ \text{s.t.} \quad & \boldsymbol{g} \in \Omega \end{aligned} \tag{7}$$

Formally, the global solution, denoted as $\boldsymbol{g}^*$, yields the lowest objective value,

$$f(\boldsymbol{g}^* \mid \boldsymbol{\omega}) \leq f(\boldsymbol{g} \mid \boldsymbol{\omega}), \quad \forall \boldsymbol{g} \in \Omega. \tag{8}$$

On the other hand, the outer optimization problem searches through the domain of $\boldsymbol{\omega}$, denoted as $\mathbb{S}$, in a BnB fashion. Let $f(\boldsymbol{g}^* \mid \boldsymbol{\omega})$ denotes the lowest objective value in (7) for a given $\boldsymbol{\omega}$, the search of the optimal $\boldsymbol{\omega}$ can be expressed as

$$\underset{\boldsymbol{\omega}\in\mathbb{S}}{min} \quad f(\boldsymbol{g}^* \mid \boldsymbol{\omega}), \tag{9}$$

and similarly,

$$f(\boldsymbol{g}^* \mid \boldsymbol{\omega}^*) \leq f(\boldsymbol{g}^* \mid \boldsymbol{\omega}) \quad \forall \boldsymbol{\omega} \in \mathbb{S}. \tag{10}$$

The solutions $\boldsymbol{\omega}^*$ and $\boldsymbol{g}^*$ are guaranteed to be globally optimal if and only if both problems (7) and (9) are solved globally. As mentioned, (7) is a convex problem in which the result is always globally optimal. The outer problem (9) is solved globally with BnB, which the details are elaborated in the following section.

3.2 Branch-and-bound (BnB)

Branch-and-Bound is used to search through the $\mathbb{S}$ space in a divide and conquer manner. In short, our algorithm branches the search space into smaller sub-spaces and prune them using two efficient bounding functions. Specifically, when $\boldsymbol{\omega}$ is given as an uncertainty region, $\mathbb{B}$ (details in Section 3.3.2), an upper bound and a lower bound of the objective value are required to determine if the region should be searched further. The searching stops when the gap between the bounds, τ, diminished, which indicates that the global solution (up to τ, which is set to a small value for numerical reasons) is found.

3.3 Bounding functions

We first state the requirements and functions of the bounds. The upper bound must fulfil the following condition:

$$\overline{\overline{f}} \geq \ f(\boldsymbol{g}^* \mid \boldsymbol{\omega}^*), \tag{11}$$

which is achieved with any sub-optimal solution. We set it to the current lowest objective value, $f(\boldsymbol{g}^* \mid \hat{\boldsymbol{\omega}})$ (Algorithm 2, line 26), which will decrease progressively each time a better solution is found.

The lower bound, on the other hand, must fulfil the following condition:

$$\underline{\underline{f}}(\boldsymbol{g}^* \mid \mathbb{B}) \leq \min_{\boldsymbol{\omega} \in \mathbb{B}} \ f(\boldsymbol{g}^* \mid \boldsymbol{\omega}), \tag{12}$$

which the derivation is much more involved. Besides, it has to converge to $f(\boldsymbol{g} \mid \boldsymbol{\omega})$ as $\mathbb{B}$ collapses to a single point,

$$\underline{\underline{f}}(\boldsymbol{g}^* \mid \mathbb{B}) \to f(\boldsymbol{g}^* \mid \boldsymbol{\omega}) \text{ when } \mathbb{B} \to \boldsymbol{\omega}. \tag{13}$$

See Horst & Tuy (2013)'s work (chap. 4) for a detailed explanation behind these conditions. In a nutshell, if the lower bound error of a local region $\mathbb{B}$ is higher than the current upper bound error, it implies the absence of the optimal $\boldsymbol{\omega}^*$ in this local region, which can be pruned away safely (see Fig. 2).

There are two prerequisites bounds in the path to deriving $\underline{\underline{f}}(\boldsymbol{g}^* \mid \mathbb{B})$. We first draw attention to the fact that the coefficient matrix $\mathbf{A}$ in equation (6) is a function of $\boldsymbol{\omega}$. More specifically, each entry of A is a composition of two functions, expressing the (1) scattering law and (2) the relationship of the triplets: surface normal, illuminating, and observing directions. The ripple effects of having $\boldsymbol{\omega}$ as an uncertainty region $\mathbb{B}$ throughout the chain of functions will be detailed in the following subsections.

3.3.1 *Bounding the coefficient matrix, A*

Let a_{ij} represents each element of $\mathbf{A}$, expressing the relationship between the scattering law S_i, phase angle α_i, and albedo ϖ_j. Following Kaasalainen & Torppa (2001), we adopt the linear combination of Lommel-Seeliger (LS) and Lambert (L) models as the scattering law of the object, formulated as

$$a_{ij} = S_i(\mu^{(ij)}, \mu_0^{(ij)}, \alpha_i)\varpi_j, \tag{14}$$

Algorithm 2 Proposed method

Require: $\boldsymbol{l} \in \mathbb{R}^I$, $\mathbf{N} \in \mathbb{R}^{3\times J}$, P, τ, ζ.
1: Uniformly subdivide $\mathbb{S}$ into K sub-patches $\mathbb{B}_1$, ..., $\mathbb{B}_k$.
2: **for** k = 1,...,K **do**
3: $\quad\boldsymbol{\omega}_c^k \leftarrow$ Centre of $\mathbb{B}_k$.
4: $\quad$Obtain $f_k(\boldsymbol{g}^* \mid \boldsymbol{\omega}_c^k)$ by solving P_2 in (42)
5: $\quad$Obtain $\underline{\underline{f_k}}(\boldsymbol{g}^* \mid \mathbb{B}_k)$ by solving P_3 in (43)
6: **end for**
7: $k^* = argmin(\{f_k\}_{k=1}^K)$.
8: $\hat{\boldsymbol{\omega}} \leftarrow \boldsymbol{\omega}_c^{k^*}$, $\overline{\overline{f}} \leftarrow f(\boldsymbol{g}^* \mid \hat{\boldsymbol{\omega}})$
9: $q \leftarrow$ Initialise priority queue.
10: Insert $\{\mathbb{B}_k\}_{k=1}^K$ into q with priority $\underline{\underline{f_k}}(\boldsymbol{g}^* \mid \mathbb{B}_k)$.
11: Sort the q entries that share the same $\underline{\underline{f_k}}(\boldsymbol{g}^* \mid \mathbb{B}_k)$ with $f_k(\boldsymbol{g}^* \mid \boldsymbol{\omega}_c^k)$.
12: **while** q is not empty **do**
13: $\quad\mathbb{B} \leftarrow$ De-queue top item from q.
14: $\quad$Insert $\mathbb{B}$ into t.
15: $\quad$**while** t is not empty **do**
16: $\quad\quad\mathbb{B} \leftarrow$ De-queue top item from t.
17: $\quad\quad$Uniformly subdivide $\mathbb{B}$ into 4 sub-patches $\mathbb{B}_1$, ..., $\mathbb{B}_4$.
18: $\quad\quad$**for** k = 1,..., 4 **do**
19: $\quad\quad\quad\boldsymbol{\omega}_c^k \leftarrow$ Centre of $\mathbb{B}_k$.
20: $\quad\quad\quad$Obtain $f_k(\boldsymbol{g}^* \mid \boldsymbol{\omega}_c^k)$ by solving P_2 in (42)
21: $\quad\quad\quad$Obtain $\underline{\underline{f_k}}(\boldsymbol{g}^* \mid \mathbb{B}_k)$ by solving P_3 in (43)
22: $\quad\quad\quad$**if** $f(\boldsymbol{g}^* \mid \hat{\boldsymbol{\omega}}) - \underline{\underline{f}}(\boldsymbol{g}^* \mid \mathbb{B}_k) \leq \tau$ **then**
23: $\quad\quad\quad\quad$Terminate.
24: $\quad\quad\quad$**end if**
25: $\quad\quad\quad$**if** $f_k(\boldsymbol{g}^* \mid \boldsymbol{\omega}_c^k) \leq \overline{\overline{f}}$ **then**
26: $\quad\quad\quad\quad\hat{\boldsymbol{\omega}} \leftarrow \boldsymbol{\omega}_c^k$, $\overline{\overline{f}} \leftarrow f(\boldsymbol{g}^* \mid \hat{\boldsymbol{\omega}})$
27: $\quad\quad\quad$**end if**
28: $\quad\quad\quad$**if** $\underline{\underline{f_k}}(\boldsymbol{g}^* \mid \mathbb{B}_k) \leq \overline{\overline{f}}$ and $\delta\lambda > \zeta$ and $\delta\beta > \zeta$ **then**
29: $\quad\quad\quad\quad$Insert $\mathbb{B}_k$ into t with $\underline{\underline{f}}(\boldsymbol{g}^* \mid \mathbb{B}_k)$
30: $\quad\quad\quad$**end if**
31: $\quad\quad$**end for**
32: $\quad$**end while**
33: **end while**
34: Obtain $\boldsymbol{g}^*$ by solving P_2 in (42) with $\hat{\boldsymbol{\omega}}$.
35: $\boldsymbol{h} \leftarrow$ Minkwoski minimization($\boldsymbol{g}^*$, $\mathbf{N}$).
36: V, $G \leftarrow$ convex hull determination($\boldsymbol{g}^*$, $\boldsymbol{h}$, $\mathbf{N}$).
37: **return** $\hat{\boldsymbol{\omega}}$ as $\boldsymbol{\omega}^*$, V, G;

where the combination of LS and L models is

$$\begin{aligned} S_i\left(\mu^{(ij)}, \mu_0^{(ij)}, \alpha_i\right) &= f(\alpha_i)\left[S_{\text{LS}}\left(\mu^{(ij)}, \mu_0^{(ij)}\right) + c\, S_{\text{L}}\left(\mu^{(ij)}, \mu_0^{(ij)}\right)\right] \\ &= f(\alpha_i)\,\mu^{(ij)}\,\mu_0^{(ij)}\left(\frac{1}{\mu^{(ij)} + \mu_0^{(ij)}} + c\right), \end{aligned} \tag{15}$$

where the $f(\alpha_i)$ is the phase function,[2] c is a weight parameter, $\mu^{(ij)}$ and $\mu_0^{(ij)}$ are the cosine similarities between surface j ($\boldsymbol{n}_j$) of the object, and the directions of the Earth and Sun (at epoch i), respectively. They are formally expressed as

$$\begin{aligned} \mu^{(ij)} &= \boldsymbol{e}_{\text{obj}}^{(i)} \cdot \boldsymbol{n}_j, \\ \mu_0^{(ij)} &= \boldsymbol{s}_{\text{obj}}^{(i)} \cdot \boldsymbol{n}_j. \end{aligned} \tag{16}$$

[2] $f(\alpha) = A_0 \exp(\frac{\alpha}{D}) + k\alpha + 1$, A_0 and D are the amplitude and scale length of the opposition effect, and k is the overall slope of the phase curve.

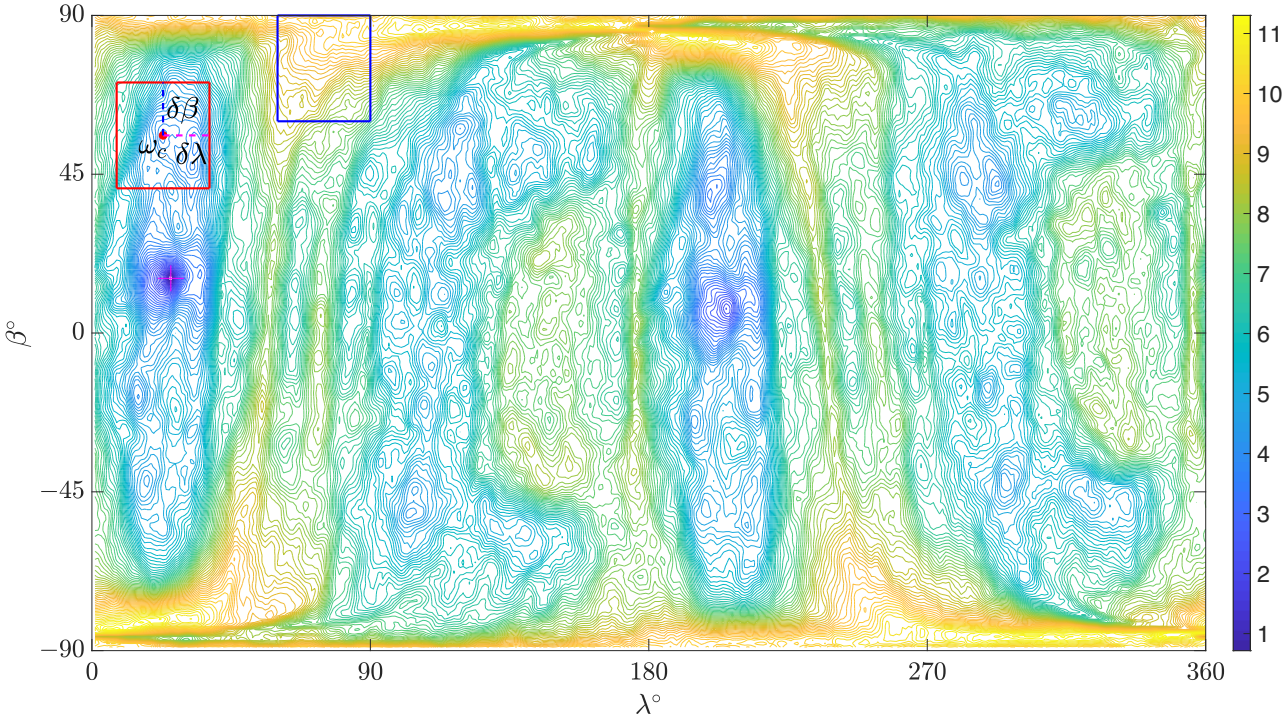

Figure 2. The domain of $\boldsymbol{\omega}$ visualized with the contour of the objective function $f(\boldsymbol{g}^* \mid \boldsymbol{\omega})$. The light curves are simulated with a rhombicuboctahedron spinning with the axis sitting at the coordinate $\lambda = 25^\circ$, $\beta = 15^\circ$ (where the global minimum is), highlighted by magenta '+'. Both the red and blue squares illustrate two sub-patches $\mathbb{B}$. Assume that the current upper bound $\overline{\overline{f}}$ is determined with the $\boldsymbol{\omega}_c$ in the red sub-patch, the blue patch then will not be branched further since the lowest error within that region, $\underline{\underline{f}}(\boldsymbol{g}^* \mid \mathbb{B}_{\text{blue}})$, is higher than the current $\overline{\overline{f}}$.

Note that the locations of the Sun($\boldsymbol{s}$) and Earth($\boldsymbol{e}$) are given in the (ecl)iptic coordinate (object-centred inertial frame). Hence, they have to be rotated to the (obj)ect's coordinate (where the z-axis is aligned with the spin pole, alongside its corresponding x and y axes). We adopt the same Euler angle rotation sequence (Z-Y-Z),

$$\boldsymbol{v}_{\text{obj}}^{(i)} = \mathbf{R}_z(\phi_0 + \frac{360^\circ}{P}(t_i - t_0))\mathbf{R}_y(90^\circ - \beta)\mathbf{R}_z(\lambda)\boldsymbol{v}_{\text{ecl}}^{(i)}, \tag{17}$$

where ϕ_0 is the initial orientation angle (with its corresponding epoch t_0), t_i represents the i-epoch, $\boldsymbol{v} \in \mathbb{R}^3$ represents the $\boldsymbol{e}$ and $\boldsymbol{s}$ vectors, and $\mathbf{R}_k(\theta)$ is a rotation matrix formed with θ with the k-axis,

$$\mathbf{R}_z(\theta) = \begin{pmatrix} \cos(\theta) & \sin(\theta) & 0 \\ -\sin(\theta) & \cos(\theta) & 0 \\ 0 & 0 & 1 \end{pmatrix}, \tag{18}$$

$$\mathbf{R}_y(\theta) = \begin{pmatrix} \cos(\theta) & 0 & -\sin(\theta) \\ 0 & 1 & 0 \\ \sin(\theta) & 0 & \cos(\theta) \end{pmatrix}. \tag{19}$$

When the Euler angles (λ and β) representing the spin pole are allowed to perturb within an uncertainty region, $\mu^{(ij)}$ and $\mu_0^{(ij)}$ naturally follow suit. Such uncertainty ripples to the top of the relationship, leading to uncertain a_{ij}. A bottom-up explanation approach will be adopted from here on, where we start from bounding $\mu^{(ij)}$ and $\mu_0^{(ij)}$ and eventually determining the interval of a_{ij}.

3.3.2 *Bounding μ and μ_0*

The construction of the search space of λ and β will first be explained, followed by the range of μ and μ_0 as a function of the size of the uncertainty region.

The entire search space of both λ and β is a 2D rectangular patch, which we denote as $\mathbb{S}$ from here on. The long sides of the patch (representing λ) range from 0° to 360°, while the short sides (representing β) ranges from -90° to 90°. Note that every point within the boundary of $\mathbb{S}$ can be mapped to a unique rotation matrix under the Z-Y-Z Euler angles rotation sequence as formulated in equation (17) if the left-most rotation matrix (i.e. $\mathbf{R}_z(\phi_0 + \frac{360^\circ}{P}(t_i - t_0))$) is replaced with an identity matrix (since it is a constant in our context). On the λ boundary of the patch, the mapping is 2-to-1 (i.e. a cyclic boundary condition, $\mathbf{R}_z(\lambda = 0^\circ) = \mathbf{R}_z(\lambda = 360^\circ)$).

The search space is then branched into smaller sub-patches as the algorithm proceeds. Each sub-patch (we denote as $\mathbb{B}$) is defined by a centre point $\boldsymbol{\omega}_c = \{\lambda_c, \beta_c\}$, along the half side-lengths $\delta\lambda$ and $\delta\beta$. The illustration of both $\mathbb{S}$ and $\mathbb{B}$ can be seen in Fig. 2.

Given a sub-patch as described above, the goal is to determine the uncertainty intervals of both μ and μ_0. Note that since both μ and μ_0 share the same mathematical properties, we continue the following discussion based on μ only, where $\overline{\mu}$ denotes the upper bound, and $\underline{\mu}$ denotes the lower bound. Also, the indices are removed without the loss of generality for the sake of compactness.

The first step is to determine how much can $\boldsymbol{e}_{\text{obj}}$ be rotated within a given patch. Thus, we first restate an important lemma in Hartley & Kahl (2009)'s work, which was used in numerous works (see Yang et al. 2015; Parra Bustos et al. 2016; Li et al. 2020; Liu, Parra & Chin 2020) as the cornerstone to derive rotation-dependence bounding functions.

LEMMA 1. *For any $\boldsymbol{v} \in \mathbb{R}^3$, let $\mathbf{R}_1$ and $\mathbf{R}_2$ be two rotations in* SO*(3), and $\angle$ be the angular distance between them, lying within the range of $0^\circ \leq \theta \leq 180^\circ$, the angular distance between the two rotated $\boldsymbol{v}$, denoted as $\mathbf{R}_1\boldsymbol{v}$ and $\mathbf{R}_2\boldsymbol{v}$, is upper bounded by the angular distance*

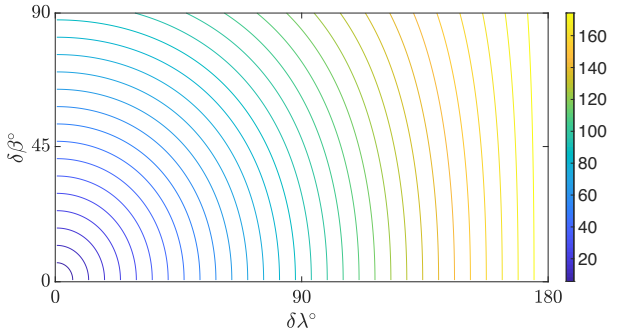

Figure 3. Contour plot of $\theta_{\max\mathbb{B}}$ as a function of $\delta\lambda$ and $\delta\beta$ with the centre point (λ_c, β_c) aligned to origin.

between $\mathbf{R}_1$ *and* $\mathbf{R}_2$*, formally as*

$$\angle(\mathbf{R}_1\boldsymbol{v}, \mathbf{R}_2\boldsymbol{v}) \leq \angle(\mathbf{R}_1, \mathbf{R}_2), \tag{20}$$

where the angular distance between two 3D vectors is expressed as $\angle(\mathbf{R}_1\boldsymbol{v}, \mathbf{R}_2\boldsymbol{v}) = \arccos((\mathbf{R}_1\boldsymbol{v})^\intercal\mathbf{R}_2\boldsymbol{v})$ *and the angular distance between two rotation matrices is expressed as* $\angle(\mathbf{R}_1, \mathbf{R}_2) = \arccos((\mathrm{trace}(\mathbf{R}_1{}^\intercal\mathbf{R}_2) - 1)/2)$*. The equality is achieved when the axis of the relative rotation* $\boldsymbol{R}_1{}^\intercal\boldsymbol{R}_2$ *is perpendicular with* $\boldsymbol{v}$*.*

Based on Lemma 1, our goal now is to compute the largest angular distance between the centre of a given patch ($\boldsymbol{\omega}_c$) and the furthest point on the patch, which we denote as $\boldsymbol{\omega}_r$ from here on. We note that the relative angular distance between two rotation matrices can be expressed in terms of their relative Euler angles with the formula below [see equations (B1) to (B13) in the supplementary appendices for the derivation],

$$\begin{aligned}\cos(\angle(\mathbf{R}_{\boldsymbol{\omega}_c}, \mathbf{R}_{\boldsymbol{\omega}_r})) &= \frac{1}{2}(1 + \cos(\beta_c - \beta_r))(\cos((\lambda_c - \lambda_r) + (\phi_c - \phi_r))) \\ &\quad + \frac{1}{2}(\cos(\beta_c - \beta_r) - 1)),\end{aligned} \tag{21}$$

where $\mathbf{R}_{\boldsymbol{\omega}_c} = \mathbf{R}_z(\phi_c)\mathbf{R}_y(90^\circ - \beta_c)\mathbf{R}_z(\lambda_c)$, and $\mathbf{R}_{\boldsymbol{\omega}_r}$ with its corresponding Euler angles. Since $\phi_c - \phi_r = 0$ in our context (no uncertainty since the spin period P is given), it is clear that $\angle(\mathbf{R}_{\boldsymbol{\omega}_c}, \mathbf{R}_{\boldsymbol{\omega}_r})$ is directly proportional to the distances between the λ and β pairs (i.e. $\beta_c - \beta_r$ and $\lambda_c - \lambda_r$) provided that the distances are not greater than 180°. We translate this result to our problem in equation (22).

$$\cos(\theta_{\max\mathbb{B}}) = \frac{1}{2}(1 + \cos(\delta\beta))(\cos(\delta\lambda)) + \frac{1}{2}(\cos(\delta\beta) - 1). \tag{22}$$

Given any sub-patch $\mathbb{B}$ from the search space $\mathbb{S}$, the maximum relative rotation angle (from $\boldsymbol{\omega}_c$), denoted as $\theta_{\max\mathbb{B}}$, is a function $\delta\beta$ and $\delta\lambda$ since they are the furthest angular distances from $\boldsymbol{\omega}_c$. Conveniently, the maximum half side-lengths ($\delta\beta$ and $\delta\lambda$) of the search space are 90° and 180°, respectively (with the full side-lengths being 180° and 360°, respectively). $\theta_{\max\mathbb{B}}$ is plotted as a function of $\delta\beta$ and $\delta\lambda$ in Fig. 3, which illustrates its monotonic property as both variables depart from the origin.

Up to this point, we have shown the maximum angular distance that $\boldsymbol{e}_{\mathrm{obj}}$ (or $\mathbf{R}_{\omega_c}\boldsymbol{e}_{\mathrm{ecl}}$ more explicitly) can cover when the spin pole is given as a patch ($\boldsymbol{\omega}_c$, $\delta\lambda$, and $\delta\beta$). We then move on to derive the upper and lower bounds of μ in the following theorem.

THEOREM 1. *(Uncertainty of the incident and scattering angles) Given a surface normal* $\boldsymbol{n} \in \mathbb{R}^3$*, a patch with* $\boldsymbol{\omega}_c$ *in its centre, and* $\theta_{\max\mathbb{B}}$ *as the maximum relative angular distance as derived earlier,*

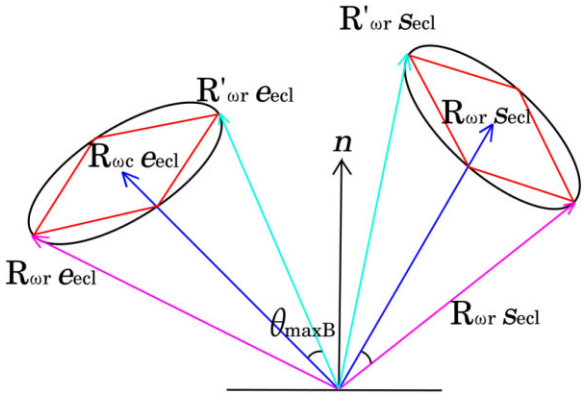

Figure 4. The construction of the uncertainty region of μ and μ_0, and consequently the range of $\mathbf{A}$. The upper bound of both μ and μ_0 is obtained by pushing the viewing and the illuminating vectors closer (represented by the cyan vectors) to the surface normal $\boldsymbol{n}$. On the other hand, the lower bounds are formed with the angles between the magenta vectors and the surface normal. The red square patches enclose the actual uncertainty regions of both vectors, which are circumscribed by the cones defined by the blue vectors and the angle $\theta_{\max\mathbb{B}}$.

the upper and lower bounds of μ *can be expressed as follows:*

$$\begin{aligned}\overline{\mu} &= \cos(\overline{\gamma}), \\ \underline{\mu} &= \cos(\underline{\gamma}),\end{aligned} \tag{23}$$

where $\overline{\gamma}$ *and* $\underline{\gamma}$ *are derived from the triangle inequalities between* $\boldsymbol{n}$*,* $\mathbf{R}_{\boldsymbol{\omega}_c}\boldsymbol{e}_{\mathrm{ecl}}$*,* $\mathbf{R}_{\boldsymbol{\omega}_r}\boldsymbol{e}_{\mathrm{ecl}}$*, and* $\mathbf{R}'_{\boldsymbol{\omega}_r}\boldsymbol{e}_{\mathrm{ecl}}$ *as follows:*

$$\begin{aligned}\angle(\mathbf{R}_{\boldsymbol{\omega}_r}\boldsymbol{e}_{\mathrm{ecl}}, \boldsymbol{n}) &\leq \angle(\mathbf{R}_{\boldsymbol{\omega}_c}\boldsymbol{e}_{\mathrm{ecl}}, \boldsymbol{n}) + \angle(\mathbf{R}_{\boldsymbol{\omega}_c}\boldsymbol{e}_{\mathrm{ecl}}, \mathbf{R}_{\boldsymbol{\omega}_r}\boldsymbol{e}_{\mathrm{ecl}}) \\ &\leq \angle(\mathbf{R}_{\boldsymbol{\omega}_c}\boldsymbol{e}_{\mathrm{ecl}}, \boldsymbol{n}) + \theta_{\max\mathbb{B}} := \underline{\gamma},\end{aligned} \tag{24}$$

$$\begin{aligned}\angle(\mathbf{R}'_{\boldsymbol{\omega}_r}\boldsymbol{e}_{\mathrm{ecl}}, \boldsymbol{n}) &\geq \angle(\mathbf{R}_{\boldsymbol{\omega}_c}\boldsymbol{e}_{\mathrm{ecl}}, \boldsymbol{n}) - \angle(\mathbf{R}_{\boldsymbol{\omega}_c}\boldsymbol{e}_{\mathrm{ecl}}, \mathbf{R}'_{\boldsymbol{\omega}_r}\boldsymbol{e}_{\mathrm{ecl}}) \\ &\geq \angle(\mathbf{R}_{\boldsymbol{\omega}_c}\boldsymbol{e}_{\mathrm{ecl}}, \boldsymbol{n}) - \theta_{\max\mathbb{B}} := \overline{\gamma},\end{aligned} \tag{25}$$

and equality is achieved when all three mentioned vectors lie on the same plane.

Proof. When $\boldsymbol{n}$ is not encapsulated within the uncertainty region, $\mathbf{R}'_{\boldsymbol{\omega}_r}\boldsymbol{e}_{\mathrm{ecl}}$ and $\mathbf{R}_{\boldsymbol{\omega}_r}\boldsymbol{e}_{\mathrm{ecl}}$ represent the closest and furthest rotated $\boldsymbol{e}_{\mathrm{ecl}}$ from $\boldsymbol{n}$ in terms of angular distance. The first line of both equations (24) and (25) state the triangle inequality between them in the angular distance metric space. Utilizing Lemma 1, we replace both the second terms with their upper bounds, namely $\theta_{\max\mathbb{B}}$. □

Fig. 4 illustrates the construction of the bounds. It depicts a minimum enclosing cone formed with $\theta_{\max\mathbb{B}}$ that includes all possible $\mathbf{R}_{\boldsymbol{\omega}_r}\boldsymbol{e}_{\mathrm{ecl}}$ within $\mathbb{B}$. We highlight that it also showcases the scenario where equality of both equations (24) and (25) is achieved.

In practice, there are two exceptional cases to Theorem 1 that need to be handled: (1) when $\boldsymbol{n}$ lies within the uncertainty region, and (2) when the closest vector (or the furthest vector) in the uncertainty region is more than 90° away from $\boldsymbol{n}$. Both of them are handled in the piece-wise functions below:

$$\overline{\gamma} = \begin{cases} 0^\circ & \theta_{\max\mathbb{B}} > \angle(\mathbf{R}_{\boldsymbol{\omega}_c}\boldsymbol{e}_{\mathrm{ecl}}, \boldsymbol{n}) \\ 90^\circ & \angle(\mathbf{R}_{\boldsymbol{\omega}_c}\boldsymbol{e}_{\mathrm{ecl}}, \boldsymbol{n}) - \theta_{\max\mathbb{B}} > 90^\circ \\ \angle(\mathbf{R}_{\boldsymbol{\omega}_c}\boldsymbol{e}_{\mathrm{ecl}}, \boldsymbol{n}) - \theta_{\max\mathbb{B}} & \text{otherwise} \end{cases} \tag{26}$$

$$\underline{\gamma} = \begin{cases} 90^\circ & \angle(\mathbf{R}_{\boldsymbol{\omega}_c}\boldsymbol{e}_{\mathrm{ecl}}, \boldsymbol{n}) + \theta_{\max\mathbb{B}} > 90^\circ \\ \angle(\mathbf{R}_{\boldsymbol{\omega}_c}\boldsymbol{e}_{\mathrm{ecl}}, \boldsymbol{n}) + \theta_{\max\mathbb{B}} & \text{otherwise} \end{cases} \tag{27}$$

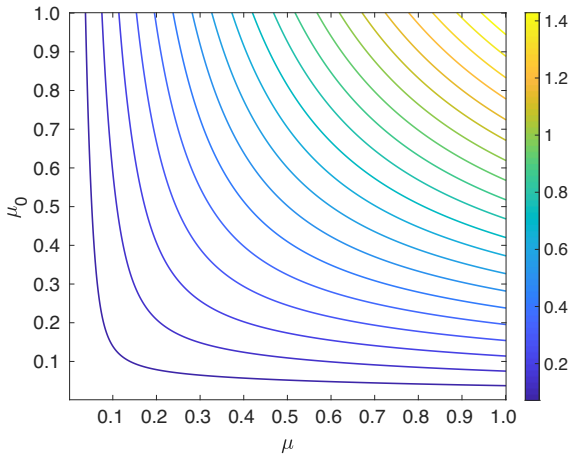

Figure 5. Contour plot of equation (14) as a function of μ and μ_0.

In words, when the uncertainty region covers $\boldsymbol{n}$ (i.e. $\theta_{\max \mathbb{B}} > \angle(\mathbf{R}_{\omega_c}\boldsymbol{e}_{\rm ecl}, \boldsymbol{n})$), the smallest angular distance is obviously 0. When $\angle(\mathbf{R}_{\omega_c}\boldsymbol{e}_{\rm ecl}, \boldsymbol{n}) > 90^\circ$, it is clipped to 90° (surface that is not facing the Earth). The same clipping range is applied to both the upper and lower bounds of γ too.

$$\begin{aligned}\overline{a}_{ij} &= S_i(\overline{\mu}^{(ij)}, \overline{\mu}_0{}^{(ij)}, \alpha_i)\varpi_j \\ \underline{a}_{ij} &= S_i(\underline{\mu}^{(ij)}, \underline{\mu}_0{}^{(ij)}, \alpha_i)\varpi_j \end{aligned} \tag{28}$$

Ultimately, we state the bound of $\mathbf{A}$ in equation (28). Intuitively, the upper bound of a_{ij} is achieved by pushing the viewing direction (and the illuminating direction) at epoch i towards surface j and distancing them for the lower bound. This aligns with the geometrical property of the Bidirectional Reflectance Distribution Function (BRDF) – the irradiance (radiance) of a particular surface is indirectly proportional to the angle between the incident (viewing) direction and the surface normal. Fig. 5 illustrates the contour plot of a_{ij} with μ and μ_0 as the axes.

This sums up the first main theorem of our paper. We highlight that this bounding function is derived based on only the scattering geometry, where the other component of the scattering law, such as the phase function (see equation 15), is a constant. Its generic property opens up potential application to other scattering laws (e.g. the Hapke model).

3.3.3 *Bounding each residual term,* $\mathrm{r_i}$

Now that each a_{ij} is allowed to perturb within a bounded range ($\underline{a}_{ij} \le a_{ij} \le \overline{a}_{ij}$), each row of $\mathbf{A}$ (denoted as $\boldsymbol{a}_i$) perturbs in an area enclosed by a hyper-disc[3] defined by the centre point $\boldsymbol{a}_i$ and the radius ρ_i,[4] where $\rho_i := \| \boldsymbol{\delta a}_i \|_2$, and $\delta a_{ij} = max(\overline{a}_{ij} - a_{ij}, a_{ij} - \underline{a}_{ij})$. As a result, there is a family of residuals given any $\boldsymbol{g}$. To formally express this, let $\boldsymbol{r} \in \mathbb{R}^I$ be the residual vector of the original problem P_0, where $r_i(\boldsymbol{g}) = | l_i - \boldsymbol{a}_i^\intercal \boldsymbol{g} |$. Now $\boldsymbol{a}_i$ is given as an uncertainty vector, $r_i(\boldsymbol{g})$ consequently exists in a range, formally as

$$r_i(\boldsymbol{g}) \in \{| l_i - (\boldsymbol{a}_i + \boldsymbol{\delta a}_i)^\intercal \boldsymbol{g} | \quad | \| \boldsymbol{\delta a}_i \|_2 \le \rho_i\}. \tag{29}$$

[3]Note that the hyper-disc is a looser region than the actual uncertainty region that we state in equation (28). It is loosen for the derivation of the residual lower bound in equation (30).

[4]Note that ρ_i is a function of the uncertainty region $\mathbb{B}$, we denote it as ρ_i instead of $\rho_i(\mathbb{B})$ here for the sake of compactness. There is no loss of generality since ρ_i can be any arbitrary number.

Recall that our main goal is to achieve $\underline{f}(\boldsymbol{g}^* \mid \mathbb{B})$, i.e. the smallest objective value in the uncertainty region $\mathbb{B}$. Hence our mission here is to derive an expression for the lower bound of (29), which leads to the second main theorem of this paper.

THEOREM 2. *(Lower bound of the residual set) For any given* $\boldsymbol{g}$*, the lower bound of the residual when* $\boldsymbol{a}_i$ *is allowed to perturb within the radius* ρ_i *is expressed as follows:*

$$\begin{aligned}&\min_{\|\boldsymbol{\delta a}_i\|_2 \le \rho_i} |l_i - (\boldsymbol{a}_i + \boldsymbol{\delta a}_i))^\intercal \boldsymbol{g}| \\ &\quad \ge max(| l_i - \boldsymbol{a}_i{}^\intercal \boldsymbol{g} | - \rho_i \ \| \boldsymbol{g} \|_2, 0) := \underline{r}_i(\boldsymbol{g} \mid \rho_i)\end{aligned} \tag{30}$$

Proof. Here we show the step-by-step derivation of (30).

$$\min_{\|\boldsymbol{\delta a}_i\|_2 \le \rho_i} | l_i - (\boldsymbol{a}_i + \boldsymbol{\delta a}_i)^\intercal \boldsymbol{g} |$$

$$= \min_{\|\boldsymbol{\delta a}_i\|_2 \le \rho_i} | (l_i - \boldsymbol{a}_i{}^\intercal \boldsymbol{g}) - \boldsymbol{\delta a}_i{}^\intercal \boldsymbol{g} | \tag{31}$$

$$\ge \min_{\|\boldsymbol{\delta a}_i\|_2 \le \rho_i} | | l_i - \boldsymbol{a}_i{}^\intercal \boldsymbol{g} | - | \boldsymbol{\delta a}_i{}^\intercal \boldsymbol{g} | | \tag{32}$$

$$\ge \min_{\|\boldsymbol{\delta a}_i\|_2 \le \rho_i} | l_i - \boldsymbol{a}_i{}^\intercal \boldsymbol{g} | - | \boldsymbol{\delta a}_i{}^\intercal \boldsymbol{g} |. \tag{33}$$

The reverse triangle inequality is first used in equation (32) to lower bound the original absolute operation. Then, in equation (33), the outer absolute operation is removed, enlarging the output space to the negative realm, which is a lower bound to the previous line. However, equation (33) is unnecessarily loose since our original problem P_0 is zero-bounded from below. Hence, we introduce a clipping operation ($max(., 0)$) to tighten the lower bound function in the derivation steps below.

$$\min_{\|\boldsymbol{\delta a}_i\|_2 \le \rho_i} | l_i - (\boldsymbol{a}_i + \boldsymbol{\delta a}_i)^\intercal \boldsymbol{g} |$$

$$\ge \min_{\|\boldsymbol{\delta a}_i\|_2 \le \rho_i} max(| l_i - \boldsymbol{a}_i{}^\intercal \boldsymbol{g} | - | \boldsymbol{\delta a}_i{}^\intercal \boldsymbol{g} |, 0) \tag{34}$$

$$\ge max(| l_i - \boldsymbol{a}_i{}^\intercal \boldsymbol{g} | - \left| \rho_i \frac{\boldsymbol{g}}{\| \boldsymbol{g} \|_2} \boldsymbol{g} \right|, 0) \tag{35}$$

$$= max(| l_i - \boldsymbol{a}_i{}^\intercal \boldsymbol{g} | - \rho_i \ \| \boldsymbol{g} \|_2, 0) \tag{36}$$

Subsequently, the upper bound of the second term in equation (34) ($\boldsymbol{\delta a}_i{}^\intercal \boldsymbol{g}$) is of interest to get RHS to its lower bound. Maximizing the dot product of two vectors ($\boldsymbol{\delta a}_i$ and $\boldsymbol{g}$) hints the leverage of the Cauchy-Schwarz inequality, which states that the upper bound is achieved when both the vectors share the same direction. Hence, $\boldsymbol{\delta a}_i$ is substituted with $\rho_i \frac{\boldsymbol{g}}{\|\boldsymbol{g}\|_2}$ in equation (35) (with ρ_i being the largest magnitude of the said direction). Subsequently, the absolute operation for the second term is removed since ρ_i is always positive, which then followed by some simple algebras to arrive at the last line. □

By minimizing the norm of the residual vector $\underline{\boldsymbol{r}}$ with its element expressed in equation (30), we are essentially solving for $\boldsymbol{g}$ that gives the smallest residual with an uncertain $\mathbf{A}$. The formal expression of the lower bound minimization problem is as follows,

$$\begin{aligned}\min_{\boldsymbol{g}} \quad & \underline{f}(\boldsymbol{g} \mid \boldsymbol{\rho}(\mathbb{B})) \\ \text{s.t.} \quad & \boldsymbol{g} \in \Omega,\end{aligned} \tag{37}$$

where $\underline{f}(\boldsymbol{g} \mid \boldsymbol{\rho}(\mathbb{B}))$ is explicitly as

$$\begin{aligned}\underline{f}(\boldsymbol{g} \mid \boldsymbol{\rho}(\mathbb{B})) &= \| \underline{\boldsymbol{r}}(\boldsymbol{g} \mid \boldsymbol{\rho}(\mathbb{B})) \|_p \\ &= \left(\sum_{i=1}^{I} (max(| l_i - \boldsymbol{a}_i(\boldsymbol{\omega}_c)^\intercal \boldsymbol{g} | - \rho_i(\mathbb{B}) \| \boldsymbol{g} \|_2, 0))^p \right)^{\frac{1}{p}}.\end{aligned} \tag{38}$$

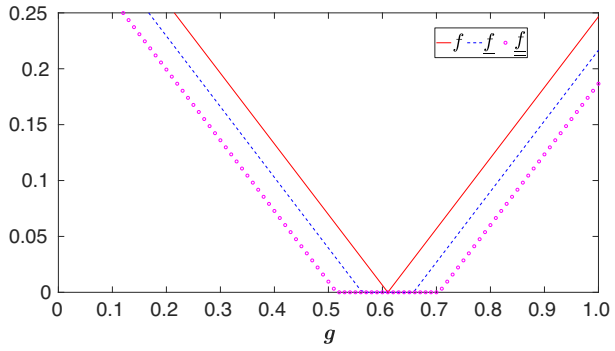

Figure 6. A 2D illustration of the original objective function $f(\boldsymbol{g} \mid \boldsymbol{\omega})$ and two of its underestimators $\underline{f}(\boldsymbol{g} \mid \rho_i(\mathbb{B}))$ and $\underline{\underline{f}}(\boldsymbol{g} \mid \rho_i(\mathbb{B}), \eta)$. Note that $\underline{f}(\boldsymbol{g} \mid \rho_i(\mathbb{B}))$ is only convex in 1D.

Note that problem (37) is similar to the robust least-squares (RLS) problem (El Ghaoui & Lebret 1997), with the main difference being RLS aims to optimize for the upper bound of the residual instead.

3.4 Convexity of the lower bound minimization problem

The global minimum of problem (37) is guaranteed only if the objective function is convex. Unfortunately, the subtraction of the quadratic term stands in the way of convexity. To circumvent this, we introduce (1) a linear under-estimator to equation (30), (2) and a quadratic constraint to the solution space of $\boldsymbol{g}$. The details and rationales of the solution are explained in the theorem below.

THEOREM 3. *(Linear underestimator of the lower bound of the residual set) Let* $\underline{\underline{r_i}}$ *be*

$$\underline{\underline{r_i}}(\boldsymbol{g} \mid \rho_i, \eta) = max(\mid l_i - \boldsymbol{a}_i{}^{\intercal}\, \boldsymbol{g} \mid \, - \eta\, \rho_i, 0), \tag{39}$$

then, $\underline{\underline{r_i}}(\boldsymbol{g} \mid \rho_i, \eta) \leq \underline{r_i}(\boldsymbol{g} \mid \rho_i) \quad \forall \boldsymbol{g} \in \{\boldsymbol{g} \in \mathbb{R}^J \mid \parallel \boldsymbol{g} \parallel_2 \leq \eta, \boldsymbol{g} \in \Omega\}$.

Proof. It is trivial to see that for any $\boldsymbol{g}$ with its 2-norm smaller (or, equal to) than η, the second term of equation (39) is always larger (or, equal to) than (30). □

By replacing the residual function in (38) with our new result (Theorem 3), the problem is formulated as below

$$\begin{aligned} P_1 : \min_{\boldsymbol{g}} \quad & \underline{\underline{f}}(\boldsymbol{g} \mid \boldsymbol{\rho}(\mathbb{B}), \eta) \\ \text{s.t.} \quad & \boldsymbol{g} \in \Gamma, \end{aligned} \tag{40}$$

similarly, $\underline{\underline{f}}(\boldsymbol{g} \mid \boldsymbol{\rho}(\mathbb{B}), \eta)$ is explicitly as

$$\begin{aligned} \underline{\underline{f}}(\boldsymbol{g} \mid \boldsymbol{\rho}(\mathbb{B}), \eta) &= \parallel \underline{\underline{\boldsymbol{r}}}(\boldsymbol{g} \mid \boldsymbol{\rho}(\mathbb{B}), \eta) \parallel_p \\ &= \left(\sum_{i=1}^{I} (max(\mid l_i - \boldsymbol{a}_i(\boldsymbol{\omega}_c)^{\intercal} \boldsymbol{g} \mid - \eta \rho_i(\mathbb{B}), 0))^p \right)^{\frac{1}{p}}, \end{aligned} \tag{41}$$

where $\Gamma = \{\boldsymbol{g} \in \mathbb{R}^J \mid \parallel \boldsymbol{g} \parallel_2 \leq \eta, \mathbf{N}\boldsymbol{g} = \boldsymbol{0}, \boldsymbol{g}_j \geq 0, j = 1, ..., J\}$. In words, the goal now is to minimize the underestimator of the lower bound function (30). Trivially, the optimized objective value in (41) (denoted as $\underline{\underline{f}}(\boldsymbol{g}^* \mid \boldsymbol{\rho}(\mathbb{B}), \eta)$) is lower than (or, equal to) (38) (denoted as $\underline{f}(\boldsymbol{g}^* \mid \boldsymbol{\rho}(\mathbb{B}))$), which implies the fulfillment of the lower bound requirement (12). We refer to Fig. 6 for the visual comparison between all three objective functions over $\boldsymbol{g}$.

Now the next crucial proof needed is the convexity of problem P_1. There are three main components: (1) the convexity of the objective function $\underline{\underline{f}}(\boldsymbol{g} \mid \boldsymbol{\rho}(\mathbb{B}), \eta)$, (2) the newly added quadratic constraint does not yield a non-convex feasible region, and (3) it does not exclude the optimal solution to the original problem P_0.

LEMMA 2. $\underline{\underline{f}}(\boldsymbol{g} \mid \boldsymbol{\rho}(\mathbb{B}), \eta) = \parallel max(\mid \boldsymbol{l} - \mathbf{A}\, \boldsymbol{g} \mid - \eta\, \boldsymbol{\rho}(\mathbb{B}), \boldsymbol{0}) \parallel_p$ *is a convex function of* $\boldsymbol{g}$.

Proof. In order to prove the lemma above, it is necessary to prove that each of the operations preserves convexity (see *Convex Optimization* by Boyd et al. 2004, chap. 3). We note that all the following operations preserve convexity:

(i) the underlying linear function of $\boldsymbol{g}$, i.e. $\boldsymbol{l} - \mathbf{A}\, \boldsymbol{g}$,
(ii) the absolute norm operation of the first term, i.e. $\mid \boldsymbol{l} - \mathbf{A}\, \boldsymbol{g} \mid$
(iii) the subtraction of a convex function with a constant, i.e. $\eta\, \boldsymbol{\rho}(\mathbb{B})$,
(iv) the point-wise maximum between two convex functions, i.e. $\mid \boldsymbol{l} - \mathbf{A}\, \boldsymbol{g} \mid - \eta\, \boldsymbol{\rho}(\mathbb{B})$ and $\boldsymbol{0}$,
(v) the outer p-norm operation. □

LEMMA 3. *All three constraints of problem* P_1 *form a convex feasible region.*

Proof. First, we prove that all the constraints are convex functions (which define convex sets). Then, we utilize the fact that the intersection of convex sets yields a convex set (see *Convex Optimization* by Boyd et al. 2004, chap. 2).

Both $\boldsymbol{g} \geq 0$ and $\mathbf{N}\boldsymbol{g} = \boldsymbol{0}$ are linear constraints, hence, are convex functions. The newly added quadratic constraint can be rewritten as $\|\boldsymbol{g}\|_2 - \eta \leq 0$. Note that all norm operations preserve convexity, which yield the first term, $\|\boldsymbol{g}\|_2$, a convex function. Subtraction of a convex function with a constant η yields another convex function.

Since all the constraints are convex constraints (defining convex sets), and the intersection of convex sets is a convex set, it is sufficient to prove that the intersection of these regions is not empty. It is trivial to see that all these regions contain the origin, $\{\boldsymbol{0}\}$ (i.e. $\boldsymbol{g} = \boldsymbol{0}$ fulfill all three constraints), hence, the intersection set contains at least the origin, which is not empty. □

LEMMA 4. *Let* $\boldsymbol{g}^*$ *be the global solution in* Ω. *There exists a positive scalar* η *such that* $\boldsymbol{g}^* \in \Omega \cap \Gamma$.

Proof. We note that the feasible region defined by Γ expands as η increases. Hence, as η approaches infinity, the constraint essentially cover the entire domain space of $\boldsymbol{g}$, which has to cover $\boldsymbol{g}^*$. □

We provide an illustration of the feasible region of $\boldsymbol{g}$ in 2D in Fig. 7. The intersection region lies on the red line ($\mathbf{N}\boldsymbol{g} = \boldsymbol{0}$) within the blue circle ($\|\boldsymbol{g}\|_2 \leq \eta$).

Here we conclude that the lower bound of the objective value, $\underline{\underline{f}}(\boldsymbol{g}^* \mid \mathbb{B})$, is achieved by solving P_1 in (41). The global minimum is guaranteed owing to its convexity property. The above sums up the second main result of this work. Note that although both of the presented theorems couples as one lower bound function for our BnB, we highlight that both of them can be employed individually. On the one hand, Theorem 1 (Uncertainty of the incident and scattering angles) can be leveraged to determine the ranges of the incident and scattering angles when the orientation of the surface is uncertain. On the other hand, Theorem 3 (Linear under-estimator of the lower

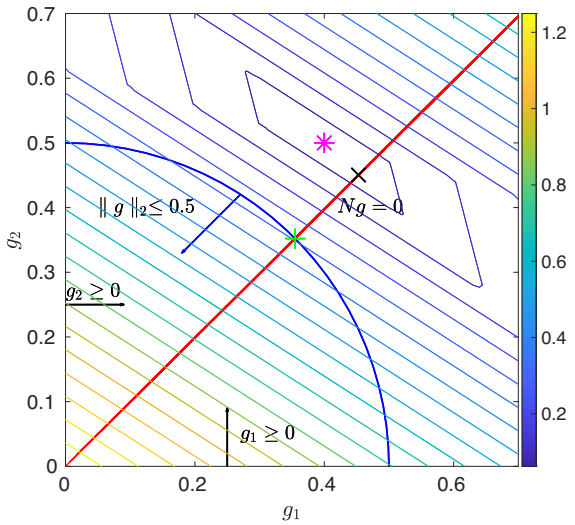

Figure 7. A 2D illustration of the feasible region with the constraints in problem P_1 (40). The contours lines represent the lower bound objective function equation (41). Three constraints are represented as (i) the non-negative constraint of $\boldsymbol{g}$ is visualized by the two black arrows, (ii) the convex shape constraint $\mathbf{N}\boldsymbol{g} = 0$ is depicted by the red line crossing the origin, and lastly, (iii) the inner pointing blue arrow indicating the feasible region within the blue semicircle defined by the quadratic constraint $\|\boldsymbol{g}\|_2 \leq \eta$. The overlap of three feasible regions lies on the red line within the blue semicircle. The three pointers (magenta '$*$', black 'x', and green '+') represent three optimal solutions under different constraints, (1) magenta '$*$' is the optimal solution with just constraint (i), (2) the black 'x' represents the optimal solution with constraints (i) and (ii), and (3) the green '+' is the optimal solution with all three constraints.

bound of the residual set) is useful in the context of minimizing the best case residual when there is uncertainty in the coefficient matrix of a linear residual function.

3.5 Convergence of $\underline{\underline{f}}(\boldsymbol{g}^* \mid \mathbb{B})$ towards $f(\boldsymbol{g}^* \mid \boldsymbol{\omega})$

The last important criteria of $\underline{\underline{f}}(\boldsymbol{g}^* \mid \mathbb{B})$ is that it has to converge to $f(\boldsymbol{g}^* \mid \boldsymbol{\omega})$ when $\mathbb{B}$ collapses to a singleton (condition 13). Since the sub-patch $\mathbb{B}$ gets smaller each time we branch it, $\delta\lambda$ and $\delta\beta$ reduce progressively and approach zero as a result and so does $\theta_{\max\mathbb{B}}$. Following the chain of events, the upper and lower bounds of μ converges to μ, which in turn collapsing the perturbation range of $\mathbf{A}$, and finally $\boldsymbol{\rho}$ as a function of the range of $\mathbf{A}$. When $\boldsymbol{\rho}$ converges to $\boldsymbol{0}$, it is obvious to see that the objective function of P_1 is equivalent to P_0.

3.6 Reformulation of P_0 and P_1

Since the choice of norm does not affect the convexity of both problems, we choose the L_1 norm and reformulate both problems into linear programming problems, (i.e. P_0 into P_2 and P_1 into P_3).

$$
\begin{aligned}
P_2 : \min_{\boldsymbol{g},\boldsymbol{r}} \quad & \sum_i^I r_i \\
\text{s.t.} \quad & l_i - \boldsymbol{a}_i(\boldsymbol{\omega}_c)^\intercal \boldsymbol{g} \leq r_i \,, \\
& -l_i + \boldsymbol{a}_i(\boldsymbol{\omega}_c)^\intercal \boldsymbol{g} \leq -r_i \quad \forall i, \\
& \mathbf{N}\boldsymbol{g} = \boldsymbol{0}, \\
& \boldsymbol{g}_j \geq 0 \quad \forall j.
\end{aligned} \tag{42}
$$

$$
\begin{aligned}
P_3 : \min_{\boldsymbol{g},\boldsymbol{r}} \quad & \sum_i^I r_i \\
\text{s.t.} \quad & l_i - \boldsymbol{a}_i(\boldsymbol{\omega}_c)^\intercal \boldsymbol{g} - \eta\rho_i(\mathbb{B}) \leq r_i, \\
& -l_i + \boldsymbol{a}_i(\boldsymbol{\omega}_c)^\intercal \boldsymbol{g} - \eta\rho_i(\mathbb{B}) \leq -r_i, \\
& r_i \geq 0 \quad \forall i, \\
& \mathbf{N}\boldsymbol{g} = \boldsymbol{0}, \\
& \boldsymbol{g}_j \geq 0 \quad \forall j.
\end{aligned} \tag{43}
$$

We first highlight that the convex shape constraints are enforced during the search instead of a post-hoc implementation as detailed in Kaasalainen et al. (2001)'s work. A couple of tricks were leveraged in the process of reformulation. First, since the residual vector are bounded below by zero, L_1 norm is equivalent to a summation of all elements in the residual vectors. Next, we highlight that $\boldsymbol{r}$ is now a parameter to be minimized, and introduces a set of non-linear inequality constraint $| l_i - \boldsymbol{a}_i{}^\intercal \boldsymbol{g} | \leq r_i$ for problem P_0. Fortunately, it can be linearized with a split into $l_i - \boldsymbol{a}_i{}^\intercal \boldsymbol{g} \leq r_i$ and $-l_i + \boldsymbol{a}_i{}^\intercal \boldsymbol{g} \leq -r_i$. Similar steps are applied to the residual vector within the *max* operation in problem P_1. We then replace the $max(, 0)$ operation by constraining each r_i element to be non-negative. The major change that requires more explanation is the omission of the quadratic constraint $\|\boldsymbol{g}\|_2 \leq \eta$ in (43). We detail below why the mentioned constraint can be enforced in a post-hoc manner without affecting the optimality of the solution.

LEMMA 5. *Let $\tilde{\boldsymbol{g}}^*$ be the minimizer of problem P_1 without the quadratic constraint $\|\boldsymbol{g}\|_2 \leq \eta$, and let $\hat{\boldsymbol{g}}^*$ be the minimizer with the constraint being enforced. If $\| \hat{\boldsymbol{g}}^* \|_2 = \eta$, then $\underline{\underline{f}}(\hat{\boldsymbol{g}}^* \mid \boldsymbol{\rho}(\mathbb{B}), \eta) \geq \underline{\underline{f}}(\tilde{\boldsymbol{g}} \mid \boldsymbol{\rho}(\mathbb{B}), \eta)$.*

Proof. The following axioms in the field of convex optimization can be leveraged to show that this is indeed the case.

(i) The minimizer of a convex optimization problem is always the global solution with the minimum objective value.
(ii) The objective value of a convex optimization problem strictly increases away from the global minimum.

As such, if the minimizer $\hat{\boldsymbol{g}}^*$ lies on the boundary of the constraint (i.e. $\| \hat{\boldsymbol{g}}^* \|_2 = \eta$), there are only two possibilities: (1) the global minimum happens to lie on the constraint's boundary (based on axiom 1), or (2) the global minimum lies outside of the constraint (based on axiom 2). If the second scenario is true, its objective value has to be higher than the minimizer obtained without the constraint, $\tilde{\boldsymbol{g}}^*$. □

The implication of Lemma 5 is that the quadratic constraint ($\|\boldsymbol{g}\|_2 \leq \eta$) can be enforced via a constraint violation detection mechanism. In other words, if the 2-norm of the solution that we obtain from solving P_3 is less than η, the solution is optimal. Otherwise, η has to be increased, and P_3 has to be solved again. We refer to Fig. 7 to aid the understanding of Lemma 5 and its proof. The magenta '$*$' indicates the solution for the unconstrained form of problem P_1. When the $\mathbf{N}\boldsymbol{g} = \boldsymbol{0}$ constraint is in place, the black 'x' is the optimal solution. The green 'x' on the other hand represents the solution when the norm constraint ($\|\boldsymbol{g}\|_2 \leq \eta$) is added. This figure depicts the scenario where the norm constraint has excluded the solution black 'x'. As discussed, such a scenario can be easily detected by checking the 2-norm of the solution, and there is a positive η that will enlarge the feasible region to include the black 'x' (see Lemma 4). Hence, we conclude that ensuring the 2-norm of

Table 1. Comparison of both methods on the simulated light-curve data. Best results in **bold**. The averaged (avg) and (best) results over eight runs with different initial spin pole estimates are reported for KTM's method.

SNR	Shape	$L_{1\,\mathrm{abs}}$ error KTM (avg)	$L_{1\,\mathrm{abs}}$ error KTM (best)	$L_{1\,\mathrm{abs}}$ error Ours	$L_{2\,\mathrm{abs}}$ error KTM (avg)	$L_{2\,\mathrm{abs}}$ error KTM (best)	$L_{2\,\mathrm{abs}}$ error Ours	Spin vector error (°) KTM (best)	Spin vector error (°) Ours
–	Cube	6.5019	0.7351	**0.0072**	0.4472	0.0512	**0.0006**	0.8062	**0.0087**
	Cuboid	60.0885	0.6134	**0.035**	4.0992	0.0427	**0.003**	0.1	**0.0087**
	House	12.4994	0.2245	**0.012**	0.8738	0.0152	**0.001**	0.2	**0.0087**
	Rhombi.	4.6472	2.6091	**0.0021**	0.3266	0.1841	**0.0002**	179.8	**0.0019**
50	Cube	8.9137	2.5767	**2.4151**	0.5015	0.1731	**0.1691**	0.9	**0.7319**
	Cuboid	64.1378	9.8968	**9.7723**	4.3414	**0.6553**	0.6695	**0.1**	0.217
	House	13.3325	2.9868	**2.9283**	0.9255	**0.1931**	0.1985	**0.2236**	0.3016
	Rhombi.	8.9137	7.8779	**7.243**	0.5991	**0.5298**	0.5621	173.5055	**1.0621**
25	Cube	8.7606	5.2103	**5.1241**	0.5943	**0.3386**	0.3529	1.2806	**0.3689**
	Cuboid	68.9347	18.0556	**17.7927**	4.6864	**1.2031**	1.2323	**0.1**	0.1366
	House	16.5097	5.8274	**5.7197**	1.1658	**0.3887**	0.4081	1.2083	**0.221**
	Rhombi.	16.6287	16.3688	**15.1368**	1.1389	**1.122**	1.1784	**122.7271**	171.0698

the area vector solution obtained from solving P_3 to be lower than η is equivalent to solving P_1 as a whole.

3.7 Implementation details

Here we elaborate the practical details of our method. It was written mainly in Matlab R2019a. Both the LP problems (P_2 and P_3) are solved with the simplex method (Dantzig 1990) implemented by Gurobi.[5] All the experiments were run in an Ubuntu 20.04 machine with 24 Intel i9 CPU cores @3.5GHz.

We took advantage of the parallelizable trait of our algorithm to reduce runtime. We notice that the early stage of our algorithm deals with mainly uncertainty regions with large patch size (in terms of $\delta\lambda$ and $\delta\beta$), which is expected to produce 0 lower bound $\underline{f}(\boldsymbol{g}^* \mid \mathbb{B})$. Hence we first divide the entire spin pole search space into K sub-patches with its centre points being 5° apart. Since the solving of P_2 and P_3 for each sub-patch has no dependence with each others, we call the 'parpool' command in Matlab and execute them (see line 2 to line 6 in Algorithm 2) in parallel with 12 workers.

Then, the queue is formed and sorted with $\underline{f}(\boldsymbol{g}^* \mid \mathbb{B})$ and $f(\boldsymbol{g}^* \mid \boldsymbol{\omega})$. Another practical observation that we made is that the optimal solution tends to *stand* in the front part of the queue. As such, we employ the depth-first search searching strategy to go through each entry of the queue (line 15 to line 32). The quicker the upper bound decreases, the more aggressive the pruning process is, which results in a faster completion speed.

Another minor trick we employed is the same straightforward parallelization to line 18 to 31. Instead of pruning at each instance (line 28), we solve P_2 and P_3 in batch and perform the pruning afterwards. We emphasize that these are not exhaustive efforts to speed up our algorithm. Highly sophisticated techniques can be employed to speed up our algorithm further (see Herrera et al. 2017).

3.8 Observational uncertainty

There are several commonly adopted methods in treating the observational uncertainty in the light-curve inversion problem. Kaasalainen et al. (2001) pointed out that the spin states and shape solutions are robust to random noise and emphasis the treatment on systematic and model errors. The authors suggested running the optimization multiple times with different initial estimates and scattering laws to get a lower bound on the error estimates. Hanuš et al. (2011) created 'mock' models based on the best-fitting model and used them to generate virtual light curves. The authors then performed inversions based on these virtual light curves to get a distribution of the spin pole. Muinonen et al. (2015) and Muinonen et al. (2020) incorporated the observation uncertainty as the weights to each of the measurement points in their optimization schemes. On the other hand, Wang et al. (2015) estimated the uncertainties of the spin parameters by using the virtual solutions method. Similar to the treatment proposed by Hanuš et al. (2011), the authors generated virtual light curves by adding Gaussian noise to the original light curves. The mode and 1-sigma of the virtual solutions' distribution are used as the spin pole prediction and the error estimate of the studied model.

Here we present two uncertainty treatments of our proposed method. First, we adopt the weighted optimization scheme of Muinonen et al. (2015) and Muinonen et al. (2020), the residual function in equation (2) takes the following form when each of the measurement uncertainty in a set of light curve (σ_i) is considered,

$$r_i = \frac{1}{\sigma_i} \left| \, l_i - \boldsymbol{a}_i^{\mathsf{T}} \boldsymbol{g} \, \right| . \tag{44}$$

In this variant, the lower bound of the residual function (equation 39) is expressed as

$$\underline{r}_i = max \left(\frac{1}{\sigma_i} \left| \, l_i - \boldsymbol{a}_i^{\mathsf{T}} \boldsymbol{g} \, \right| - \eta \rho_i(\mathbb{B}), 0 \right) . \tag{45}$$

The addition of a constant scaling term σ_i does not affect the convexity of both residual functions.

Secondly, we adopted the generic method discussed by Wang et al. (2015) in our experimental section to estimate the uncertainty in the presence of Gaussian noise.

4 EXPERIMENTAL RESULTS

We conducted several experiments to evaluate the effectiveness of our method in determining the globally optimal solution. Both

[5] https://www.gurobi.com/

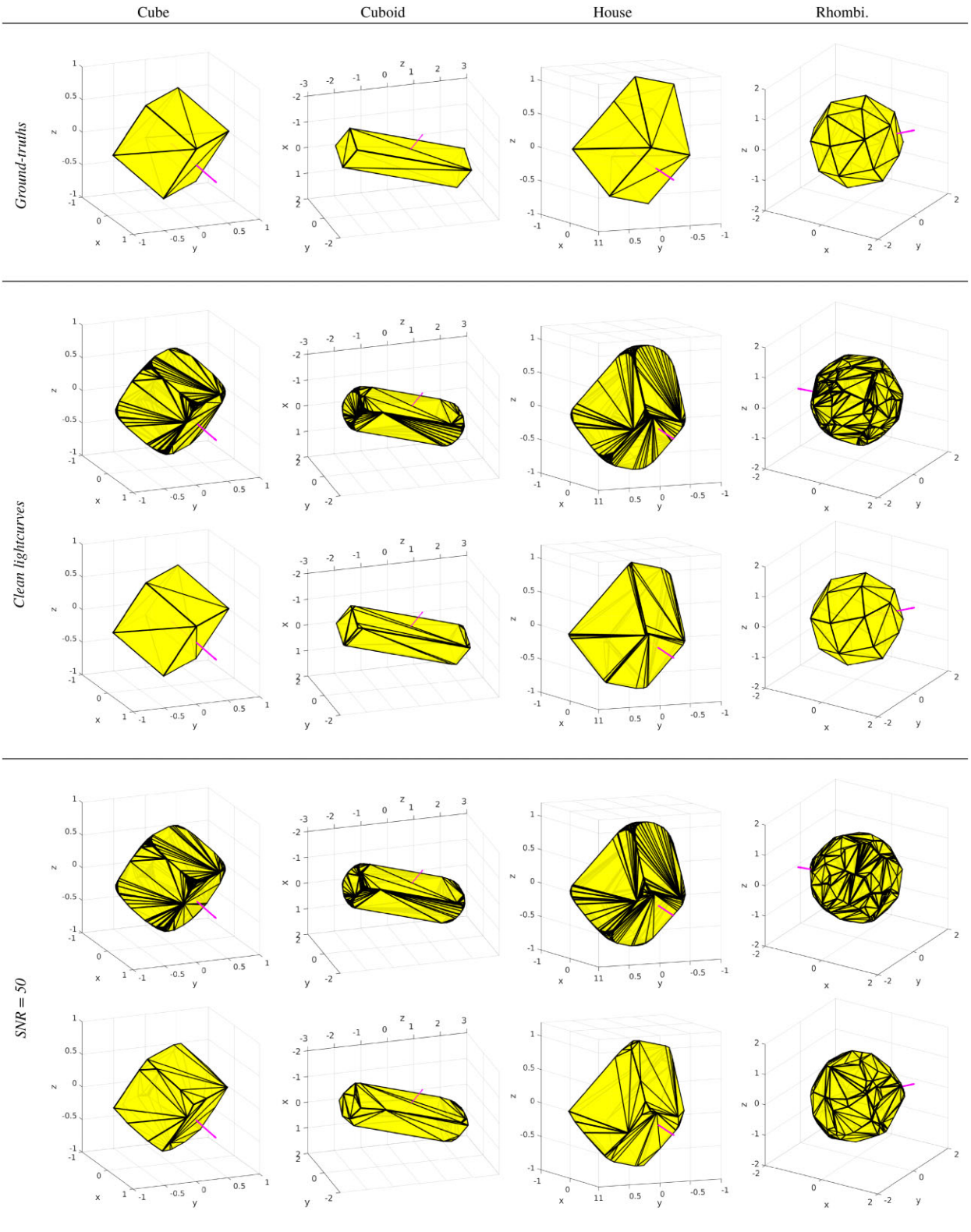

Figure 8. Visualization of the ground truths and the results of both methods (top rows: KTM's method, bottom rows: our method). From left to right: cube, cuboid, house, and rhombicuboctahedron. These polyhedrons and their respective spin poles (in pink arrow) are depicted in the ecliptic coordinate.

the simulated (with and without noise) and real light-curve data were used in the experiments. We compare against KTM's method since it is, in principle, a baseline of our method. In the real light-curve experiments, we also compare our solutions with the currently recognized models in DAMIT. This section begins with the nitty-gritty of both methods (i.e. hyperparameters and convergence criteria), followed by the metrics used in our benchmark, and lastly, the results and findings.

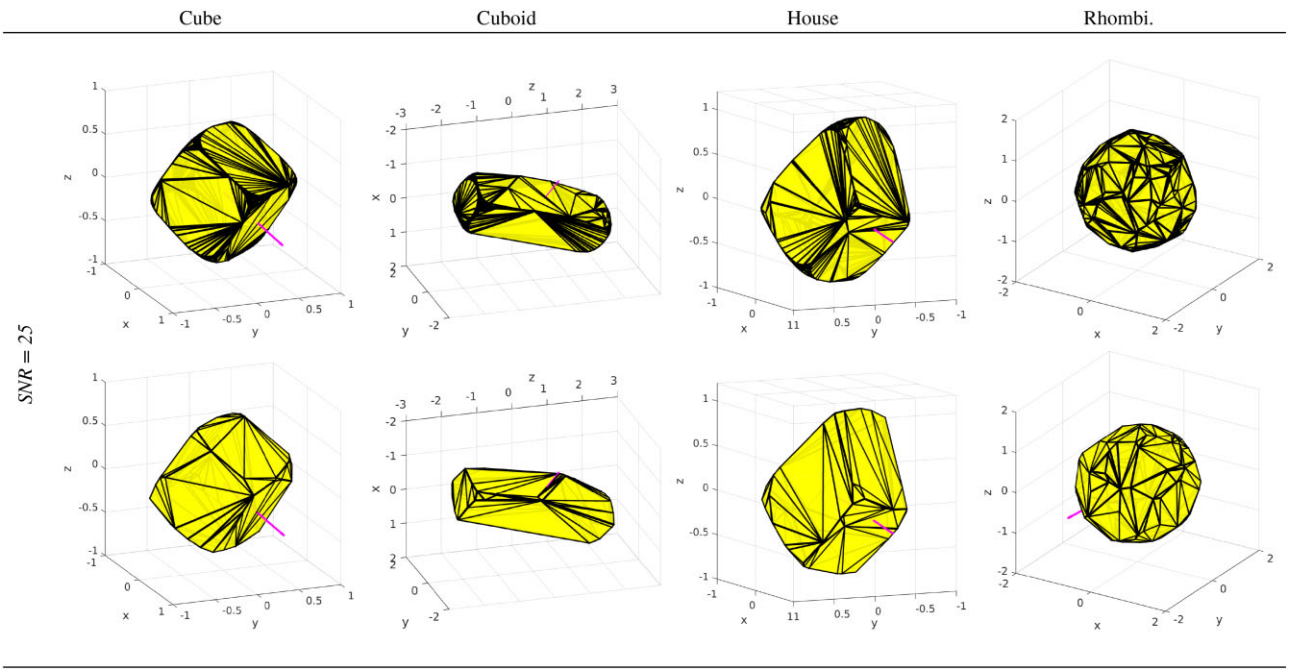

Figure 9. Continuation of Fig. 8.

Table 2. Comparison of KTM's and our method. Only the calibrated light curves are used in this controlled experiment (both as input and evaluation). The grid search variant (of our method) has the same solution and error values with our method. Best results in **bold**.

	$L_{1\text{abs}}$ error		$L_{2\text{abs}}$ error		λ°		β°		time (s)		
Asteroid	KTM	Ours	KTM	Ours	KTM	Ours	KTM	Ours	KTM	Ours	Grid search
(90265) 2003 CL5	2.6454	**1.9753**	0.1895	**0.1557**	199.9	26.4	87.1	71.72	1399	127	22176
(54827) 2001 NQ8	5.0682	**4.3125**	0.2933	**0.2718**	241.4	241.72	−47.6	−48.59	124	543	142273
	4.9865	**4.2555**	0.2872	**0.2677**	241.1	241.4	−47.6	−48.91	397	541	142322
(60744) 2000 GB93	4.9865	**2.7602**	0.3139	**0.2139**	66.8	205.16	−94.6	−69.84	255	245	59421
(56232) 1999 JM31	4.3982	**3.3958**	0.265	**0.2261**	52.1	92.03	−78.1	−65.47	142	372	90065

Table 3. Comparison of the DAMIT models and our models on the entire set of light curves (with a combination of both calibrated and non-calibrated light curves) from real asteroids. Our models were reconstructed based on the calibrated light curves only while the comparing models used the entire set of light curves. Best results in **bold**.

Asteroid	Model	$L_{1\text{rel}}$ error	$L_{2\text{rel}}$ error	λ°	β°
(90265) 2003 CL5	1734	**9.9565**	**0.7439**	11	70
	Ours	10.4342	0.8809	26.4	71.72
(54827) 2001 NQ8	1794	**16.476**	**0.8244**	72	−49
	Ours	17.4471	0.8471	241.72	−48.59
	1795	19.5059	0.9244	242	−46
	Ours	17.9249	0.8651	241.4	−48.91
(60744) 2000 GB93	3111	**7.8543**	**0.4012**	202	−69
	Ours	9.7017	0.5328	205.16	−69.84
(56232) 1999 JM31	3125	8.1212	0.4966	190	−80
	Ours	**7.3416**	**0.4686**	92.03	−65.47

4.1 Hyperparameters and convergence criteria

4.1.1 KTM's method

The first set of hyperparameters is the degree and order of spherical harmonics for the LM solver. It is documented that setting both to 6 is a good choice, which we followed in our real light-curve experiments in Section 4.4. In the simulated light-curve experiments (Section 4.3), we empirically found that 15 produces better results.

The second hyperparameter is the number of unit vectors we sample for EGI, which is needed for both solvers in KTM's method and our method. In the simulated light-curve experiments, we set it to 288 (6 rows per octant as described in the documentation) + X,

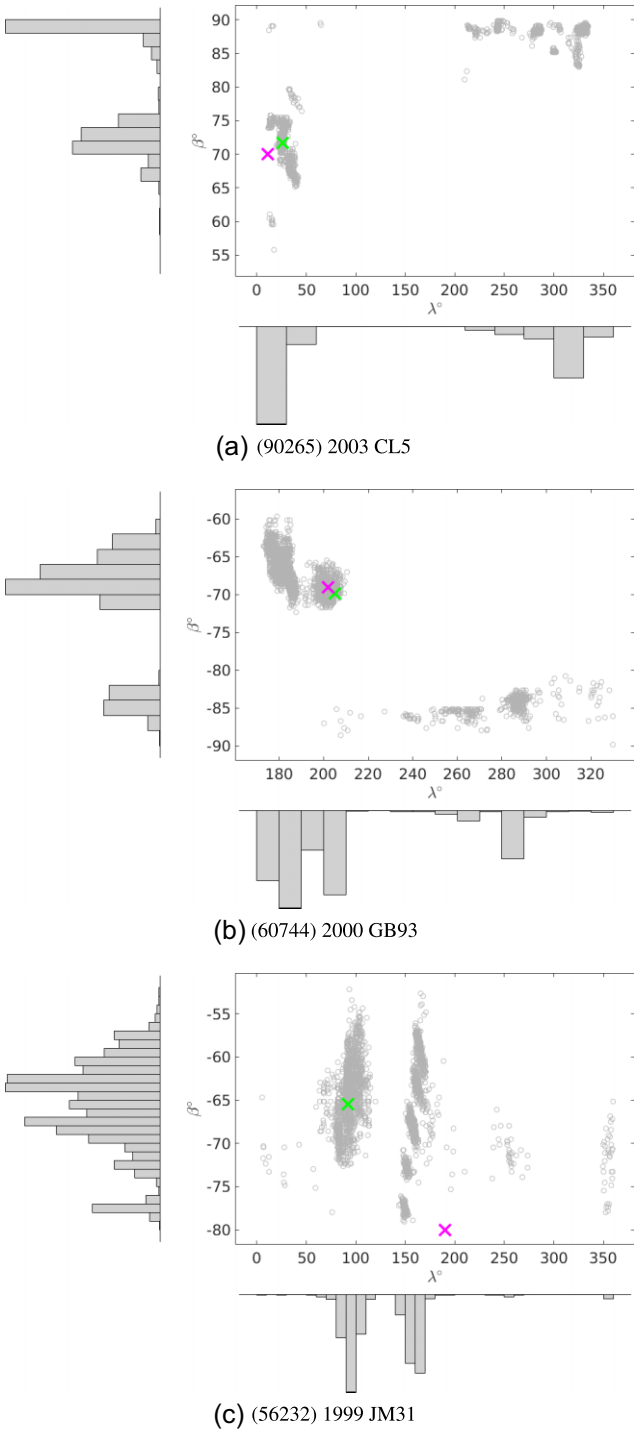

Figure 10. Spin pole distributions of the virtual solutions. Legends: Grey 'o' represents the virtual solutions, magenta and green 'x' represent the DAMIT models and our optimal models, respectively.

where X is the number of facets that the current estimating shape possesses. The surface normal of the current shape is included (in the matrix $\mathbf{N}$) so that the globally optimal area and spin pole solution is associated with zero residual, which is the best evidence for the global minimum. In the real light-curve experiments, we again follow the recommendation by the algorithm's documentation, setting it to 800 unit vectors (10 rows per octant).

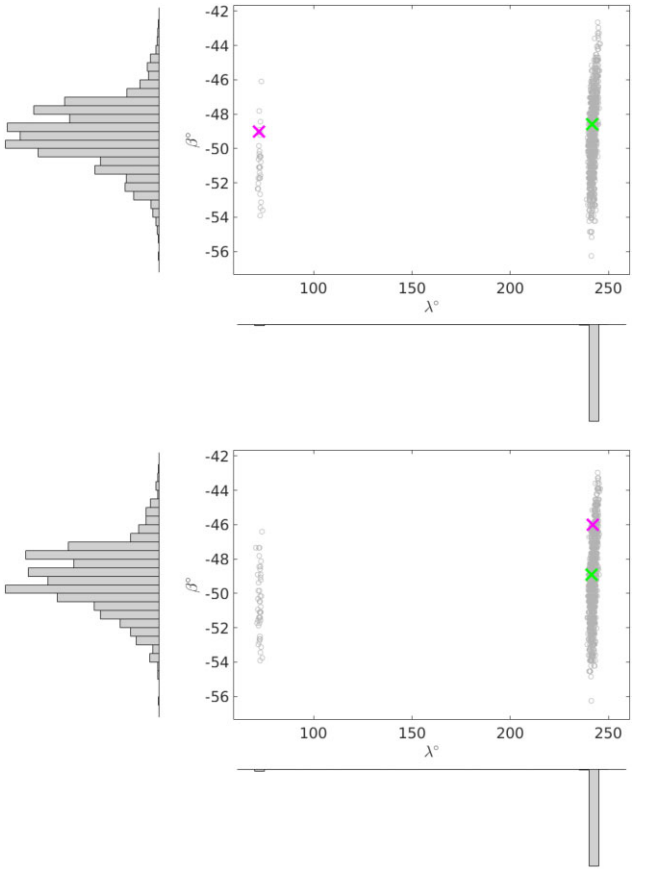

Figure 11. Continuation of Fig. 10 for (54827) 2001 NQ8. Top figure depicts the distribution with the scattering parameters of model 1794, and the bottom figure corresponds to model 1795.

We ran KTM's method as we have described in Section 1 – getting the best outcome out of eight different runs with the initialization scheme proposed by the authors. The initial estimates of the spin poles are $\lambda = \{45°, 135°, 225°, 315°\}$, $\beta = \{45°, -45°\}$, evenly distributed across the entire domain. Note that all other parameters (e.g. spin period, scattering parameters etc.) apart from the spin pole and the area vectors are fixed. We allowed both solvers to be run until convergence, i.e. the discrepancy of the objective values between consecutive iterations is smaller than 10^{-11} in all our experiments.

4.1.2 Our method

There are three hyperparameters in our method – τ, ζ, and η. The termination threshold for the discrepancy between the upper bound and the lower bound is denoted as τ, while ζ represents the smallest patch size before we stop branching a particular region $\mathbb{B}$. We set τ to 10^{-11}, and ζ is set to 0.01° for the simulated light-curve experiments and 0.28° for the real light-curve experiments. On the other hand, η is a part of the lower bound equation (equation 30); it was chosen according to the problem at hand. We start with a small value ($\eta = 2$) and increase it if the optimal solution is excluded (as explained in Section 3.4). For the simulated data experiments, the η for cube, cuboid, house, and rhombicuboctahedron are 3, 11, 5, and 3.2, respectively. For the real data experiments, $\eta = 2$ is found to be sufficient to include all optimal solutions.

4.2 Metrics

When only calibrated light curves are involved, we report the $L_{1\,\mathrm{abs}}$ and $L_{2\,\mathrm{abs}}$ fitting errors as they are the objective functions in our and KTM's method, respectively. $L_{1\,\mathrm{abs}}$ error is expressed as

$$L_{1\,\mathrm{abs}}\ \mathrm{error} = \sum_{i=1}^{I} \left| l_{\mathrm{mea}}^{(i)} - l_{\mathrm{est}}^{(i)} \right|, \tag{46}$$

and the $L_{2\,\mathrm{abs}}$ error, also known as the least-squares error, is expressed as

$$L_{2\,\mathrm{abs}}\ \mathrm{error} = \sqrt{\sum_{i=1}^{I} \left(l_{\mathrm{mea}}^{(i)} - l_{\mathrm{est}}^{(i)} \right)^2}, \tag{47}$$

where $\boldsymbol{l}_{\mathrm{mea}}$ and $\boldsymbol{l}_{\mathrm{est}}$ are the measured and the estimated light-curve, respectively.

When comparing with the DAMIT models, we report the relative errors $L_{1\,\mathrm{rel}}$ and $L_{2\,\mathrm{rel}}$ since (1) the entire set of light curve is used where there is a mix of both calibrated and relative light curves, and (2) the models in DAMIT are scaled to unit volume. The main difference between the relative and the absolute metrics is that the mean magnitude of each light-curve set is scaled to unity. As such, the absolute magnitude information is removed, which implies that two same convex shapes with different scales will produce the same light curve. Formally, $L_{1\,\mathrm{rel}}$ and $L_{2\,\mathrm{rel}}$ are expressed below,

$$L_{1\,\mathrm{rel}}\ \mathrm{error} = \sum_{w=1}^{W} \sum_{i=1}^{I} \left| \frac{l_{\mathrm{mea}}^{(wi)}}{\hat{l}_{\mathrm{gt}}^{(w)}} - \frac{l_{\mathrm{est}}^{(wi)}}{\hat{l}_{\mathrm{est}}^{(w)}} \right|, \tag{48}$$

$$L_{2\,\mathrm{rel}}\ \mathrm{error} = \sqrt{\sum_{w=1}^{W} \sum_{i=1}^{I} \left(\frac{l_{\mathrm{mea}}^{(wi)}}{\hat{l}_{\mathrm{gt}}^{(w)}} - \frac{l_{\mathrm{est}}^{(wi)}}{\hat{l}_{\mathrm{est}}^{(w)}} \right)^2}, \tag{49}$$

where $\hat{l}_{\mathrm{mea}}^{(w)}$ and $\hat{l}_{\mathrm{est}}^{(w)}$ represent the mean brightness in w-th set of light curve in the measurement and estimation, respectively.

As for the spin vector error, we compute the relative rotation distance with

$$\angle(\mathbf{R}_{\mathrm{gt}}, \mathbf{R}_{\mathrm{est}}) = \arccos((\mathrm{trace}(\mathbf{R}_{\mathrm{gt}}{}^{\intercal}\mathbf{R}_{\mathrm{est}}) - 1)/2), \tag{50}$$

where $\mathbf{R}_{\mathrm{gt}}$ and $\mathbf{R}_{\mathrm{est}}$ are formed with Euler rotation angle sequence (Z-Y-Z) as expressed in equation (17) with the corresponding λ and β (the left-most $\mathbf{R}_z$ is replaced with identity matrix). The lower is better for all the aforementioned metrics.

4.3 Simulated light-curve experiments

We used the light-curve simulator and the implementation of KTM's method from the DAMIT data base. Four different convex polyhedrons were generated – cube, cuboid, house, and rhombicuboctahedron. The spinning poles were randomly generated. Since we assume that these bodies rotate with a fixed axis, we ensure that each spinning pole aligns with the correct principal inertia axis. We sampled 328 timestamps and the locations of the Sun and Earth from the real light curve of the asteroid Ariadne (from DAMIT) for all the light curves that we simulated.

4.3.1 Light curve without noise

Given clean light curves, our method manages to converge to practically 0 objective value (see Table 1) with the correct spin poles (see fig. C1 in the supplementary appendices for the spin pole estimates of both methods) for all shapes. The numbers align with the reconstructions as depicted in Figs 8 and 9. Note that the shapes and their spin poles are visualized in the ecliptic coordinate system. These results showcase the ability of our method in converging to globally optimal solutions. We report both the average and the best error metrics of KTM's method to show its reliance on initialization. Besides, we report that the degree and order of spherical harmonics series has an influence on the convergence of KTM's method too. We found that when setting it lower than 15 (the maximum hard threshold in the software), most of the runs converged to worse solutions.

Rhombicuboctahedron is the most complex shape among the four shapes. The best spin pole solution of KTM's method is in the opposite direction of the ground-truth spin pole, which is reflected in the spin vector error column of Table 1 (179.8°). As a result, it has the highest fitting errors ($L_{1\,\mathrm{abs}} = 2.61$ and $L_{2\,\mathrm{abs}} = 0.18$) among

Table 4. Spin pole uncertainty estimates from the virtual solutions. The mean spin pole ($\tilde{\lambda}$ and $\tilde{\beta}$) and 1-σ error estimate are obtained from the major solution clusters, see Figs 10 and 11 and text for more references.

Asteroid	Pole	$\tilde{\lambda}^\circ$	$\tilde{\beta}^\circ$
(90265) 2003 CL5	1	71.9 ± 2.56	26.84 ± 4.87
(54827) 2001 NQ8	1*	72.49 ± 0.49	−50.73 ± 1.67
	2*	242 ± 0.92	−49.18 ± 1.73
	1#	72.41 ± 0.64	−50.52 ± 1.88
	2#	242.07 ± 0.95	−49.14 ± 1.76
(60744) 2000 GB93	1	181.66 ± 4.41	−66.33 ± 2.32
	2	201.81 ± 2.65	−69.38 ± 1.92
(56232) 1999 JM31	1	93.27 ± 7.33	−64.31 ± 3.68

Notes. *Scattering parameters of model 1794.
#Scattering parameters of model 1795.

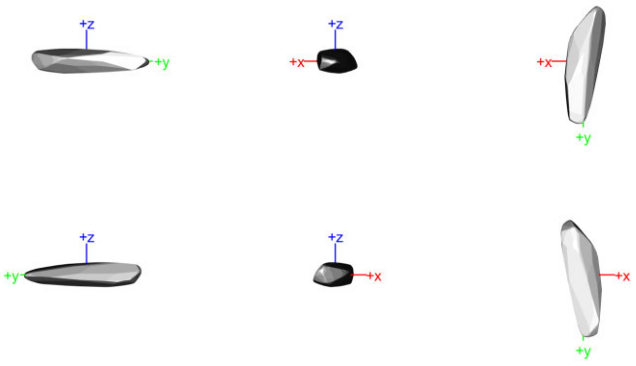

(a) Model 1734, $\lambda = 10°, \beta = 70°$.

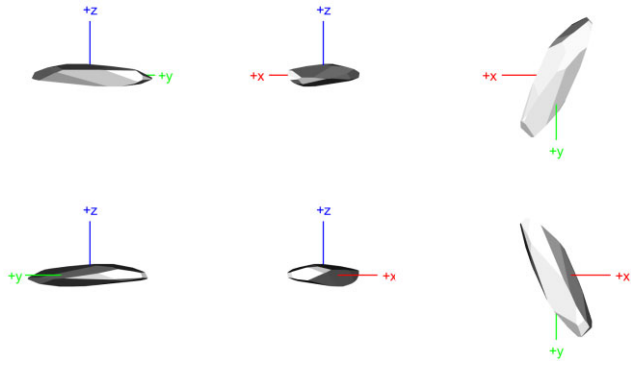

(b) Our model, $\lambda = 24.84°, \beta = 74.22°$.

Figure 12. Convex shape models of asteroid (90265) 2003 CL5.

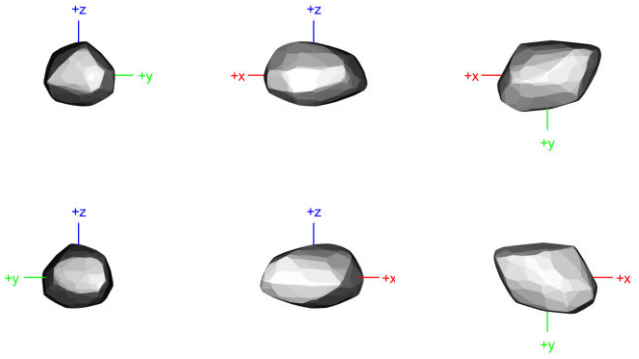

(a) Model 1794, $\lambda = 72°, \beta = -49°$.

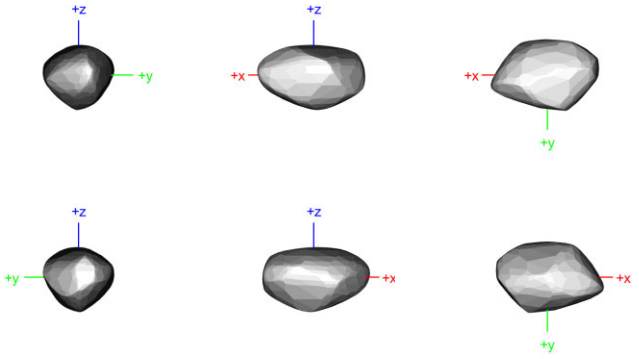

(b) Model 1795, $\lambda = 242°, \beta = -46°$.

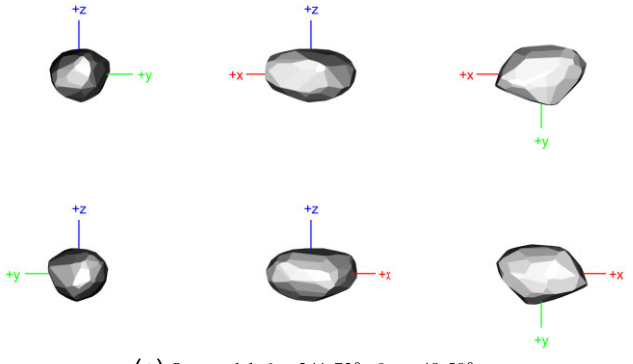

(c) Our model, $\lambda = 241.72°, \beta = -48.59°$.

Figure 13. Convex shape models of asteroid (54827) 2001 NQ8.

all comparing shapes. In order to verify that this is the failure of KTM's method (specifically, the LM solver) in converging to the global minimum, we ran a controlled experiment where we ran the LM solver under two different settings. In the first setting, we fixed the spin pole parameters to the ground-truth and solve for only the Gaussian surface density. In the second one, we initialize the LM solver with evenly distributed spin poles as described earlier and solve for both the spin pole and the Gaussian surface density. We found that the shape solution from the first setting is significantly better than the second setting, i.e. $L_{1\text{abs}}$: 0.9518 versus 3.3763 and $L_{2\text{abs}}$: 0.0714 versus 0.2324, which clearly indicates that the LM solver fails to converge to the better set of spin pole and shape solutions when the spin pole parameters are not fixed. Interestingly, one of the runs in the second setting, initialized closest to the ground-truth, converged to $\lambda = 29.8°$, $\beta = 15.1°$ (ground-truth spin pole is $\lambda = 25°$, $\beta = 15°$), with a slightly higher fitting errors ($L_{1\text{abs}} = 3.7955$ and $L_{2\text{abs}} = 0.2654$) than the best solution. This experiment proves our point that the convergence of a local method to a global minimum is not guaranteed despite an initialization strategy.

4.3.2 Light curve with noise, SNR = 25, 50

Given noisy light curves, with the signal-to-noise ratio (SNR) of 50 and 25, our method achieves the lowest $L_{1\text{abs}}$ errors in all experiments. This result is consistent with our previous results, showcasing the ability of our method in achieving global minimum. Note that the global minimum in the $L_{1\text{abs}}$ space does not correspond to the global minimum in the $L_{2\text{abs}}$ space; this explains the lower $L_{2\text{abs}}$ errors of KTM's method.

The convex shapes and the spin pole orientations of both methods closely resemble the ground-truths of the cube, cuboid, and house shapes. These results demonstrate the robustness of light-curve inversion against random noise in the measurements, which aligns with Kaasalainen & Torppa (2001)'s findings.

Lastly, we highlight that there are a lot of local minima in the residual space of rhombicuboctahedron, as illustrated in the four big *valleys* in Fig. 2. We associate this to the symmetrical property of the shape, and the low inclination orbital plane (Kaasalainen & Lamberg 2006). When there is random noise in the light curves, one of these local minima in the clean light curves turns into the global minimum, which explains the large discrepancies between the ground-truth spin poles and the solutions of our method. In such cases, the spin vector error is not a meaningful comparison metric.

4.4 Real light-curve experiments

Real light-curve experiments were conducted to examine the practical aspects of our method. We selected four asteroids from DAMIT with sufficient calibrated light curves for our experiments. There are three main results presented in this section. The goal of the first experiment is to validate the ability of our method in achieving the best $L_{1\text{abs}}$ fit results when given the same set of hyperparameters and calibrated light curves to both methods. Since we use only the calibrated light curves, we compare the solutions with the absolute light-curve fitting errors (i.e. $L_{1\text{abs}}$ and $L_{2\text{abs}}$), see Table 2. In the second experiment, we present the comparisons between our models and the currently recognized models in DAMIT (obtained with KTM's method by different authors). One major difference between the two is that the DAMIT models were inverted based on a larger set of light curve (both calibrated and non-calibrated). In this experiment, we compare both methods on the entire set of available light curves, which consists of both calibrated and non-calibrated light curves. As such, we use the relative fitting errors $L_{1\text{rel}}$ and $L_{2\text{rel}}$ metrics in the comparison, see Table 3.

In both of the experiments, we adopted the same set of hyperparameters (i.e. sidereal spin period P, initial epoch t_0, initial angle ϕ_0, and light scattering parameters (amplitude a, width d, and slope k of the phase angle function for Lambert + Lommel Seeliger scattering model) that are reported in the DAMIT data base (see Section 5).

We highlight that all of the in-depth comparisons will be made on the second experiment since those models were reported by third parties and are currently recognized in the DAMIT data base. The first experiment can only be seen as a controlled experiment since the choice of the exclusive hyperparameter in KTM's method (i.e. the degree and order of spherical harmonics for the LM solver) might be sub-optimal. Nevertheless, the controlled experiment is necessary to ensure our models are indeed the global minimum solutions given the same set of light curves and common hyperparameters.

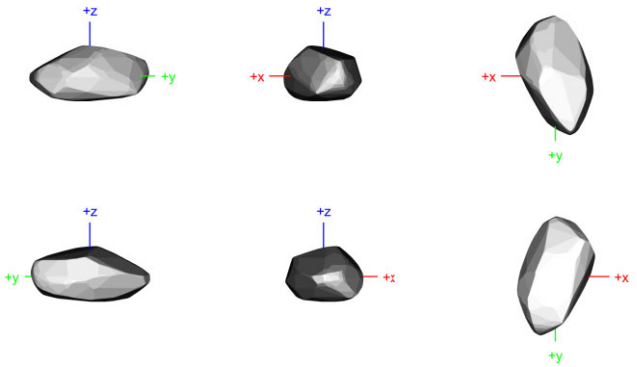

(a) Model 3111, $\lambda = 202°, \beta = -69°$.

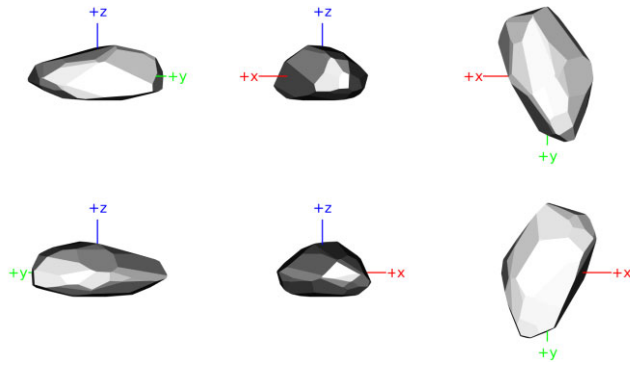

(b) Our model, $\lambda = 205.16°, \beta = -69.84°$.

Figure 14. Convex shape models of asteroid (60744) 2000 GB93.

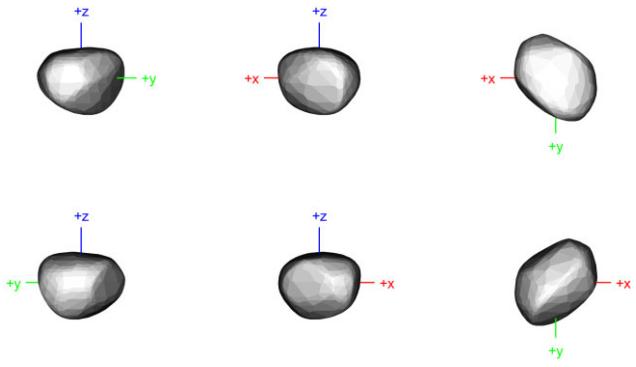

(a) Model 3125, $\lambda = 190°, \beta = -80°$.

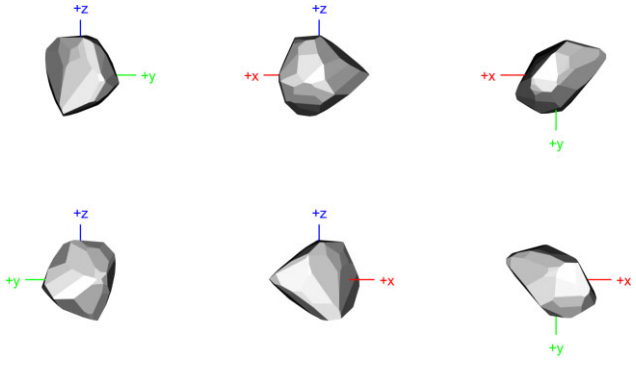

(b) Our model, $\lambda = 92.03°, \beta = -65.47°$.

Figure 15. Convex shape models of asteroid (56232) 1999 JM31.

In order to get the uncertainty estimations of both the spin pole (λ, β) and the area vector of EGI ($\boldsymbol{g}$), we performed a Monte Carlo simulation by running our method on 3000 virtual light curves for each asteroid. Following Wang et al. (2015), we added Gaussian noise to the original light curves with the standard deviation of the fitting error of our best-fitting models.

The summarization of all the results and visualization is as follows: Table 3 tabulates the fitting errors and spin pole solution, Figs 10 and 11 visualized the spin pole distributions, Table 4 tabulates the major clusters in these distributions, Figs 12–15 visualized the each reconstructed asteroid, Fig. 16 depicts the distributions of each EGI, and finally, Figs 17 and 18 illustrates the generated light-curves of each comparing model.

(90265) 2003 CL5 is one of the largest asteroids in the young Datura family. The details of its photometric observations process can be referred to in Vokrouhlickỳ et al. (2017b). The collection has 16 (out of 18) calibrated light curves which we fed into our algorithm. Our spin pole solution ($\lambda = 26.4°, \beta = 71.72°$) in general agrees with Vokrouhlickỳ et al. (2017b)'s model – model 1734 ($\lambda = 11°, \beta = 70°$). The $L_{1\text{rel}}$ and $L_{2\text{rel}}$ errors and spin pole solutions are tabulated in Table 3. The simulation results are visualized in the first row of Fig. 10. The mean and 1-σ uncertainty of the major cluster is $\lambda = 26.84° \pm 4.87$, $\beta = 71.9° \pm 2.5$, which is close to both of the comparing models. However, the spread-out distribution of the virtual solutions around the north pole region illustrates the poorly constrained nature of the light curves. Vokrouhlickỳ et al. (2017b) also reported similar findings.

Fig. 12 compares the convex shapes of both methods. The top panel of the figure is viewed from the positive axes and the bottom panel from the negative axes. The shades in the convex model figures in this paper illustrate the brightness of each surface when they are observed and illuminated from the same direction, modelled with the light scattering law in equation (14). Both convex models share the same elongated feature. The uncertainty of the EGI can be seen in the first row of Fig. 16. The unit vectors (of the EGI) in northern and Southern hemisphere are projected on the left and right polar scatter plots, respectively. Due to its dependence on the spin pole's orientation, plotting the EGI of all virtual solutions is meaningless due to the spread-out distribution of the spin pole solutions. Hence, we plot only the sets of EGI associated with the spin pole solutions that lie within the tabulated pole clusters (Table 4) to show the neighbouring solutions of our best-fitting model.

The polar scatter plots in Fig. 16 convey two information: the range of area magnitudes of each unit vector and its frequency of being 'turned on' (i.e. larger than zero). The grey 'blobs' are the products of stacking each individual solution of different sizes. The size of each unfilled circle is the product of its unique area solution and the (globally) normalized frequency of the particular unit vector. The black circles represent the EGI of our best-fitting model. They are scaled by the same normalized frequency factors as well. Consistent among the (considered) virtual and best-fitting solutions of this asteroid, the unit vectors of the second and fourth segments are being turned on more frequently with significant larger area values, which again highlights the elongated shape along its equator.

In terms of light curves fitting, model 1734 fits the measurements better, with a positive gap of 0.4777 and 0.137 in terms of $L_{1\text{rel}}$ and $L_{2\text{rel}}$, respectively. We associate this to the two missing light curves in our input subset. To better illustrate this, we plot the light curves produced by both models at various observing geometries in Fig. 17. The aforementioned missing light curves are visualized in the top row of Fig. 17, where our model has a worse fit than

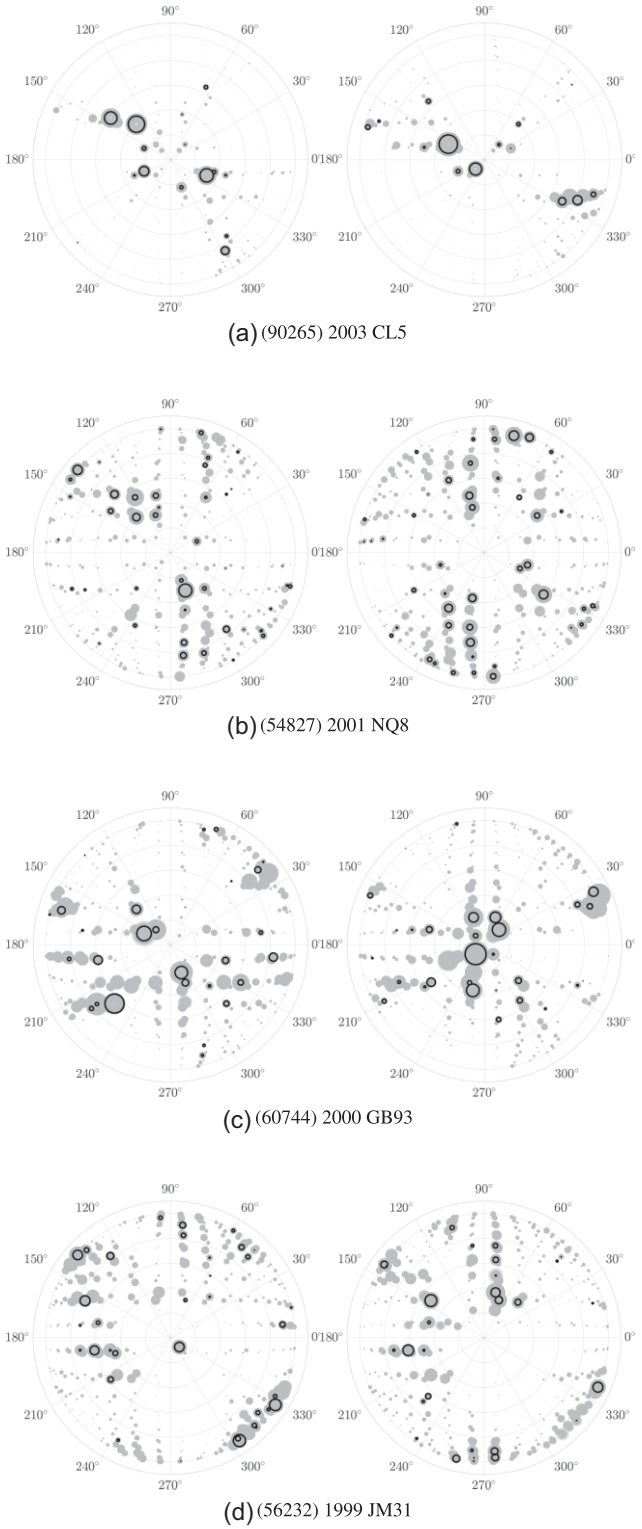

Figure 16. EGI uncertainty plots. The EGI of the virtual solutions are visualized with grey circles. The size of each circle is determined by the area magnitude and the turned on frequency of the unit vector. See the text for more details. The black circles represent the best-fitting EGI.

model 1734. The second row illustrates the contrary instead, where our model has a better fit. The light curves generated by the virtual solutions are used to generate the 1-σ error bar and envelope in the plot. Consistent with previous observations, the error bars are significantly larger in the missing light curves. The same observations are repeated in every comparison, which we omit in the rest of this section.

The results of the controlled experiment can be seen in Table 2. Our model has a better fit in both $L_{1\text{abs}}$ and $L_{2\text{abs}}$ metrics, with a positive margin of 0.6701 and 0.0338, respectively.

(54827) 2001 NQ8's details and its photometric observations process are elaborated in Vokrouhlickỳ et al. (2017a)'s work. The collection has 13 (out of 20) calibrated light curves which we used in the inversion process. Vokrouhlickỳ et al. (2017a) reported two possible solutions – model 1794 and 1795. The former's spin pole solution is $\lambda = 72^\circ$, $\beta = -49^\circ$, and the latter is $\lambda = 242^\circ$, $\beta = -46^\circ$. Both solutions are associated with different light scattering parameters. Model 1794's scattering parameters are $a = 0.44$, $d = 0.14$, $k = -0.71$, and model 1795's scattering parameters are $a = 0.36$, $d = 0.11$, $k = -0.78$. We performed inversions with both sets of scattering parameters and obtained two very similar solutions ($\lambda = 241.72^\circ$, $\beta = -48.59^\circ$ and $\lambda = 241.4^\circ$, $\beta = -48.91^\circ$). Among the four models, model 1794 has the best light curves fit, with a clear margin of 0.9711($L_{1\text{rel}}$) and 0.0227 ($L_{2\text{rel}}$) to the second-best model (our model). Model 1795 has the worst fitting errors among them. Since both of our solutions are essentially the same, we compare only one of them with the best model (model 1794) in the light curves plots (see third and fourth rows of Fig. 17).

The top and bottom distribution plots in Fig. 11 were obtained with model 1794's and model 1795's scattering parameters, respectively. There are two distinct clusters in both distributions, covering the pole solutions of both DAMIT models and our model. The uncertainty is small, i.e. less than 1° for λ, and less than 2° for β. It shows that the light curves constraint the model pretty well apart from the 180° ambiguity in λ. It is interesting that almost all the virtual solutions lie on Pole 2, i.e. $\tilde{\lambda} \approx 242^\circ$, $\tilde{\beta} \approx -49^\circ$, which is a strong indication that the calibrated light curves favour this solution.

Fig. 13 visualizes the convex shapes of three different models (model 1794 in the first row, model 1795 in the second row, and our solution with spin pole orientation $\lambda = 241.72^\circ$, $\beta = -48.59^\circ$ in the third row). Since the shapes were drawn with a fixed coordinate, we can see that model 1794 differs from model 1795 and our model by roughly a sign flip owing to the ≈180° difference in λ. The EGIs of the virtual solutions can be seen in the second row of Fig. 16. In general, the uncertainty plots indicate that the asteroid possesses surfaces of diverse directions with significant distributions on the 60° to 150° and 210° to 330° regions.

In the controlled experiment, KTM's method converge to essentially the same spin pole solution (approximately $\lambda = 241^\circ$, $\beta = -48^\circ$) with both set of scattering parameters. The result aligns with the distributions of our virtual solutions. The positive margins of our models are 0.7557(0.731) and 0.0215(0.0195) in terms of $L_{1\text{abs}}$ and $L_{2\text{abs}}$, respectively (bracket for the result with the scattering parameters of model 1795).

(60744) 2000 GB93 is the primary asteroid in the asteroid pair (60744). Its details are covered in a comprehensive asteroid pairs study by Pravec et al. (2019). 14 out of 19 of its available light curves are calibrated. We compare our solution with the only reported model – model 3111, in which the spin pole orientation is

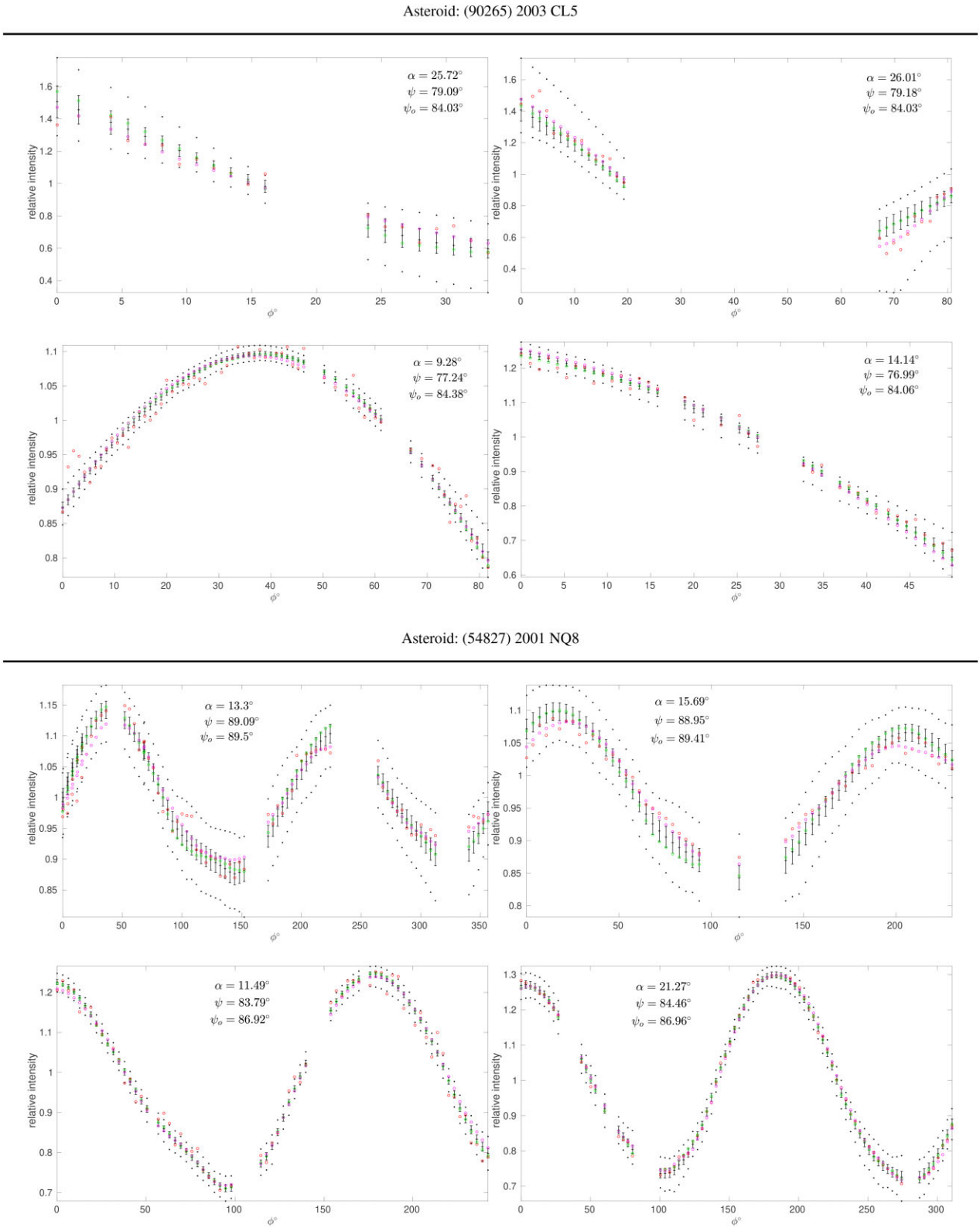

Figure 17. Real light-curve measurements and generated light curves with the DAMIT models, our best-fitting models, and the virtual solutions from our Monte Carlo simulation (see the text for details). Legends: red 'o' represent the real light-curve measurement, magenta and green 'o' represent the light curves generated by the DAMIT model and our best-fitting model, respectively. The light curves generated by the 3000 virtual solutions are used to generate the 1-σ error bar and envelope (black dots). Furthermore, α is the angle between the Sun and Earth vectors, ψ is the angle between the north pole and Earth's direction (ψ_o for the Sun's direction) in the object-centred ecliptic coordinate.

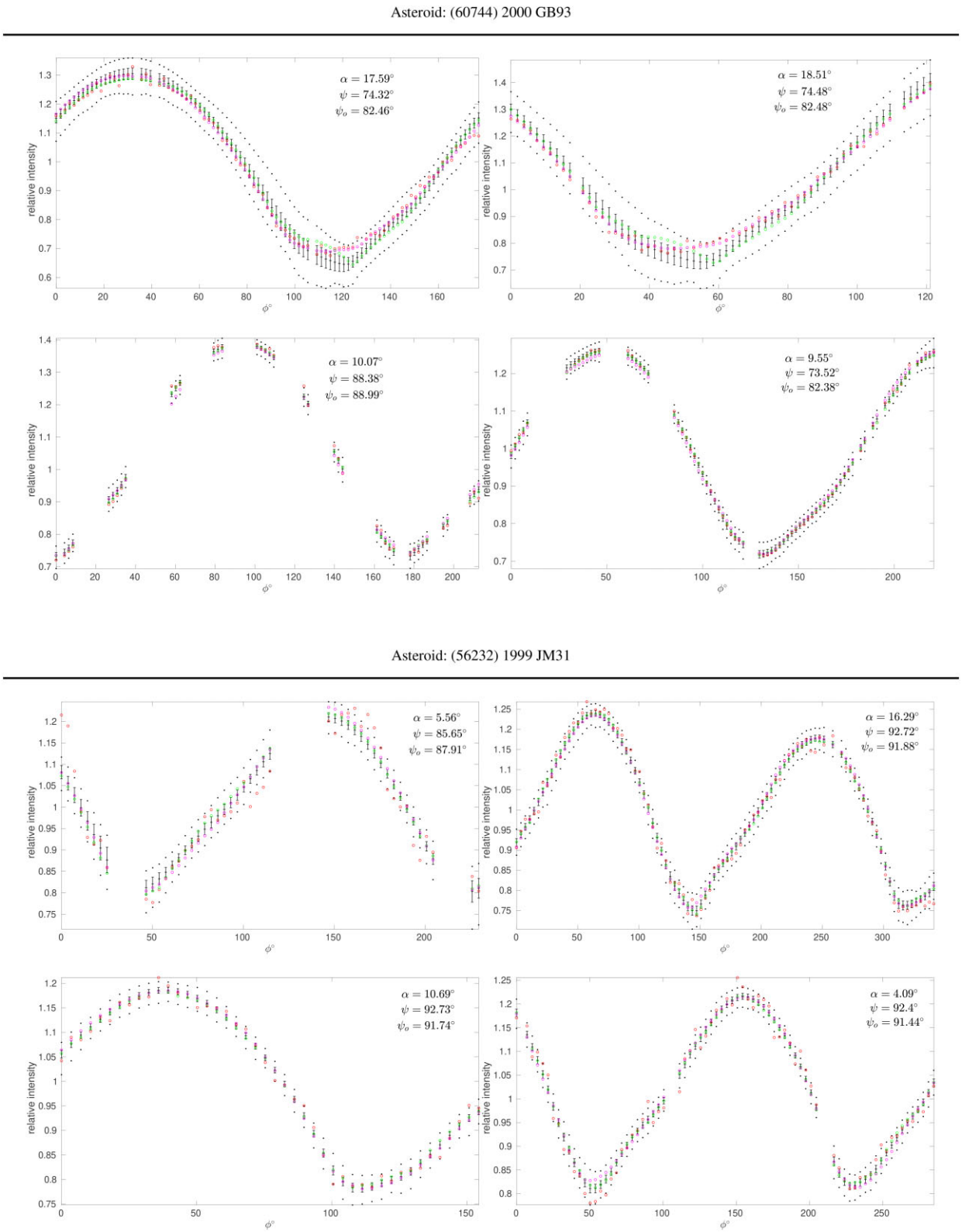

Figure 18. Continuation of Fig. 17.

$\lambda = 202°$, $\beta = -69°$. Our spin pole solution ($\lambda = 205.16°$, $\beta = -69.84°$) agrees greatly with the mentioned model. Both comparing models again lie in the same distribution (second row in Fig. 10), i.e. $\tilde{\lambda} = 201.89° \pm 2.68$, $\tilde{\beta} = -69.42° \pm 2.04$. The other significant distribution is nearby ($\tilde{\lambda} = 181.71° \pm 4.3$, $\tilde{\beta} = -69.42° \pm 2.04$), separated by a notable gap. Similar to (90265) 2003 CL5, the spread of the virtual solutions around the southern pole indicates the poor constraint nature of the light curves.

The reconstructed convex shapes of both models look alike at the coarse level (see Fig. 14), but a closer look reveals the lower level

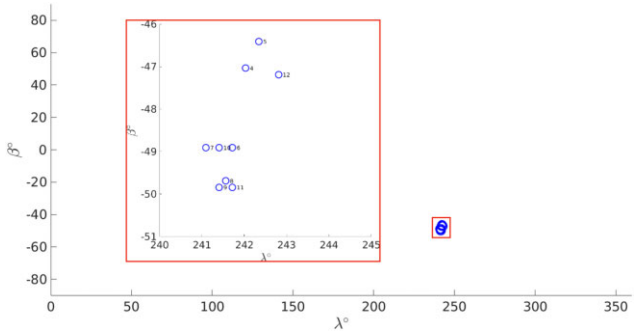

Figure 19. Spin pole distribution of (54827) 2001 NQ8 with varying EGI resolutions. The zoomed-in of the distribution is drawn on top of the entire domain.

differences, especially in z–x(middle) and y–x(right) views. The EGI plots in the third row of Fig. 16 reveal the major distributions near the asteroid's northern and southern poles. The larger equator facets can be seen in the distributions near the 30° and 210° segments. It shares a similar larger facets attribute with (90265) 2003 CL5.

With the lack of five missing light curves (with dense measurements) in our inversion process, our model has a clear negative margin of 1.8474 and 0.1316 in terms of $L_{1\mathrm{rel}}$ and $L_{2\mathrm{rel}}$, respectively. Such margins are well reflected in the first row of Fig. 18 (the missing light curves), where our model demonstrates an observable looseness with the measurements. The second row shows the contrary, where our model fits better with the light curves in our subset. In the controlled experiment, our model has clear positive margins in both absolute fitting errors, 2.2263 and 0.1 in terms of $L_{1\mathrm{abs}}$ and $L_{2\mathrm{abs}}$, respectively.

(56232) 1999 JM31 belongs to an asteroid pair as well, which is also covered in Pravec et al. (2019)'s work. 17 out of 19 of its light curves are calibrated. Again, we benchmark our method against the only reported model – model 3125, in which the spin pole orientation is $\lambda = 190°, \beta = -80°$. Our solution is $\lambda = 92.03°, \beta = -65.47°$, with a large disagreement in λ. The major cluster of the virtual solution is located at $\tilde{\lambda} = 93.36° \pm 8.67, \tilde{\beta} = -64.39° \pm 3.72$ (see third row of Fig. 10). Similarly, there is a spread of solutions ranging from $-55°$ to $-80°$ in β and $150°$ to $-170°$ in λ.

Naturally, the convex shapes of both models differ significantly as depicted in Fig. 15. The area distribution of this asteroid is crowded on the middle to equator part of the shape (see the fourth row of Fig. 16). In general, the shapes are made of smaller facets distributed in various local regions.

Both fitting errors favour our model with a positive margin of 0.7796 and 0.028 in terms of $L_{1\mathrm{rel}}$ and $L_{2\mathrm{rel}}$, respectively. In the controlled experiment, our model has a positive margin of 1.0024 and 0.0389 in terms of $L_{1\mathrm{abs}}$ and $L_{2\mathrm{abs}}$, respectively.

We highlight that both model 3125 and our model are not spinning with the correct principal inertia axis. For model 3125, the angular distance between the spin pole and the principal axis with the highest moment of inertia is approximately 35°. For our model, the offset is approximately 90°. The closest principal axis to the spin pole of our model is the axis with the second-highest moment of inertia, which is approximately 10° away.

4.4.1 *Uncertainty in the resolution of EGI*

The resolution of EGI has a direct impact on the final model of the asteroid (Kaasalainen & Torppa 2001). The recommended number

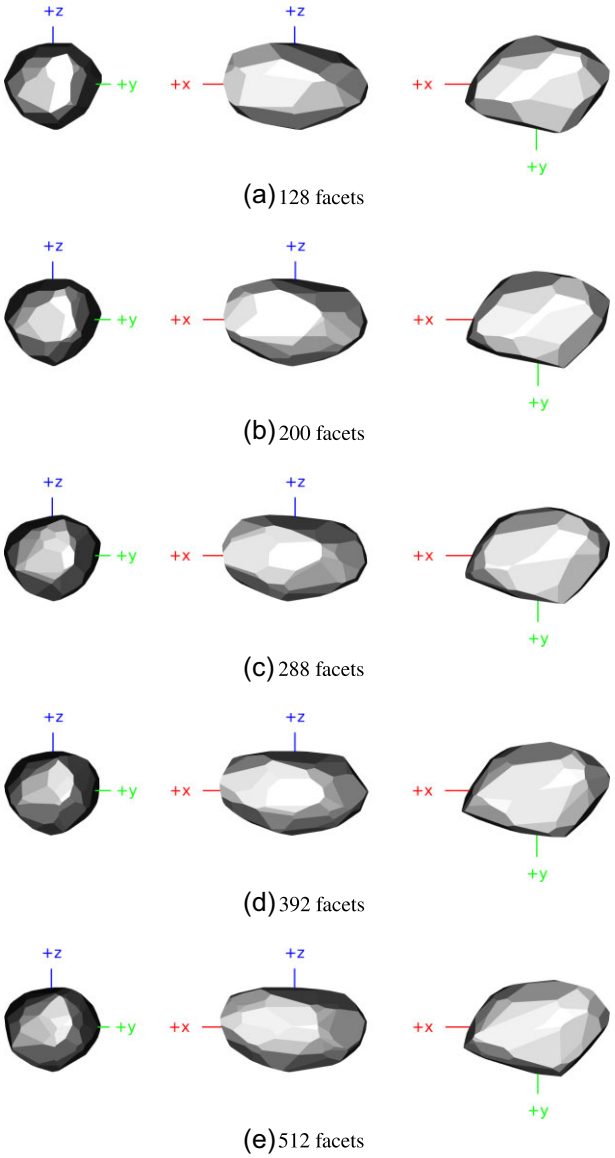

Figure 20. Convex shape models of (54827) 2001 NQ8 with varying EGI resolutions.

of rows (in each octant) in the triangulation technique proposed by Kaasalainen & Torppa (2001) ranged from 8 to 10 (higher row number for a higher resolution EGI). As such, we performed an uncertainty assessment of our models with different resolutions. Asteroid (54827) 2001 NQ8 was chosen in this experiment due to its well-constrained nature. We performed nine inversions with the number of rows in the range of 4 to 12, which corresponds to 128 to 1152 facets (i.e. $8 \times \mathrm{number\_of\_rows}^2$).

In general, all nine models possess high similarities in all observed aspects. The spin pole distribution is shown in Fig. 19, which has a similar distribution to the Monte Carlo simulation's result in Fig. 11. The largest differences in β is less than 4°, and less than 2° in λ. The overall shape with different resolutions look similar in all nine variants (see Figs 20 and 21). Not surprisingly, the detail of the surfaces gets finer as the resolution goes up. This observation is highlighted in Fig. 22, where the model with the highest resolution (in blue) has more and smaller facets than the other extreme (in

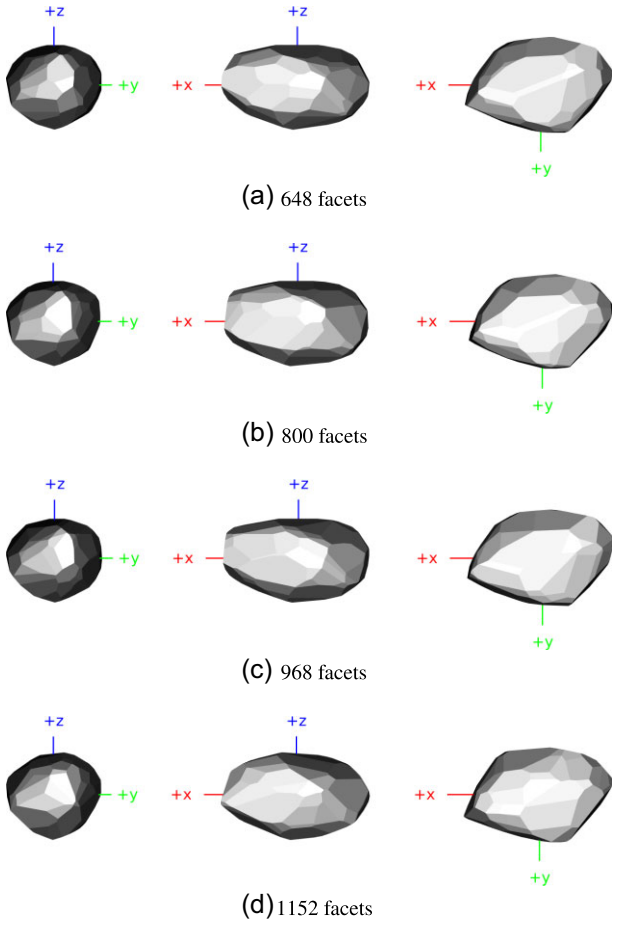

Figure 21. Continuation of Fig. 20.

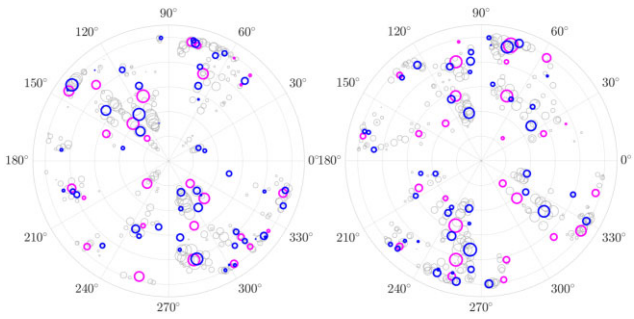

Figure 22. EGI plots of different models of (54827) 2001 NQ8 models with varying EGI resolutions. The magenta and blue circles represent the models with the least (4) and most (12) triangulated rows. All other variants are visualized with grey markers.

magenta). Last but not least, we also plotted the light curves of these models in Fig. 23. The coloured light curves highlight the extreme comparison, where the model with the highest number of facets (blue lines) has a better fit than the model with only 128 facets (magenta lines).

4.4.2 Speed

The speed of both methods is tabulated in the last column of Table 2. For KTM's method, we ran all eight runs in parallel and recorded the longest period among them. For our method, we report the time

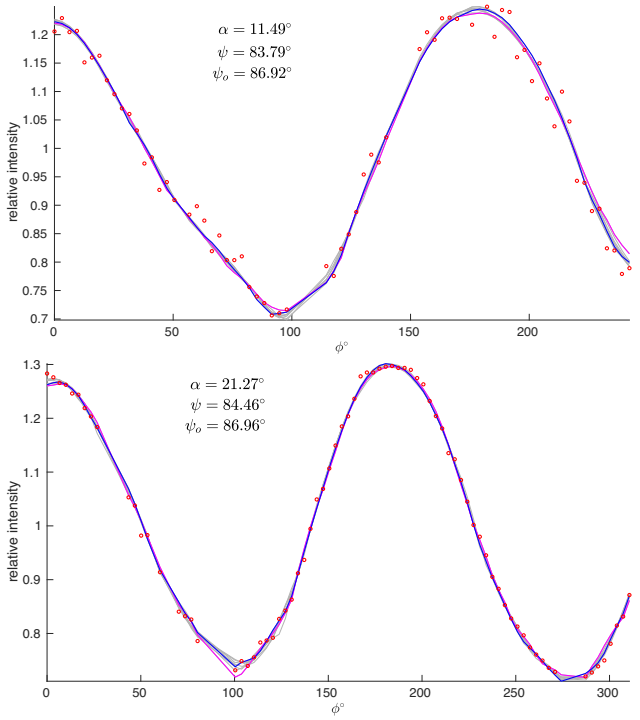

Figure 23. Generated light curves of different models of (54827) 2001 NQ8 with varying EGI resolutions. The red 'o' are the measurements, and the grey lines are the light curves of all nine models. The highlighted light curves, magenta and blue lines, represent the models with the least (4) and most (12) triangulated rows.

taken to arrive at the global solution, where no further improvement is found until the termination of our algorithm. The speed of both methods is similar in all five runs. However, we highlight that KTM's method is much faster when run in the recommended settings (i.e. terminate within a couple of hundreds of iterations) than our reported time. The cause of the slower speed reported here stems from the fact that we allowed the algorithm to run its full course (i.e. until the error plateau up to the numerical precision level) to ensure that it converges to the minimum.

Besides, we conducted an experiment to evaluate the speed gain of our algorithm compared to a naive grid search in the spin pole domain. The spin pole domain is first sampled to the precision of 0.28°, which is the same as ζ that we used in our algorithm in real light curves experiments. Then we solve P_2 [equation (42), solve for the area vector $\boldsymbol{g}$ given a spin pole $\boldsymbol{\omega}$] in parallel,[6] with each of the sampled spin poles. In short, the grid search algorithm is equivalent to solving our proposed shape inversion formulation without the BnB framework. As tabulated in the last column of Table 2, the time taken is significantly higher (hours longer) in all our conducted experiments. These results clearly indicate the efficiency of our algorithm over the naive grid search.

5 CONCLUSION

We presented a novel algorithm for estimating an object's spin pole and area vector from its light curves. Our branch-and-bound based algorithm always find the globally optimal solution in the $L_{1\,\mathrm{abs}}$

[6]With 12 workers assigned, consistent with our algorithm as explained in Section 3.7.

space and is ready to be integrated into the established light-curve inversion pipeline. By replacing the two-stage spin pole and area vector determination module in the classical light-curve inversion pipeline (KTM's method) with our proposed algorithm, the search for other unknowns of the object such as the spin period and scattering parameters can be done in a domain scanning fashion. The best set of parameters is guaranteed to be associated with the lowest $L_{1\,\mathrm{abs}}$ fitting error. In the process of designing our algorithm, we mathematically derived a novel lower bound for the element-wise light-curve fitting residual when the spin pole orientation is given as an uncertainty region. One practical advantage of our algorithm is the elimination of the initialization process. We validated our global optimality claim empirically in both simulated and real light-curve experiments. We also evaluated the practicality of our method by comparing our solutions with the currently accepted models in the DAMIT data base.

ACKNOWLEDGEMENTS

We would like to express our gratitude towards our reviewers, Karri Muinonen and Przemyslaw Bartczak, for their thorough reviews and valuable suggestions. This work is funded by the Australian Research Council (ARC) grant DP200101675. Tat-Jun Chin is SmartSat Cooperative Research Centre (CRC) Professorial Chair of Sentient Satellites.

DATA AVAILABILITY

All the light curves data and asteroid models used in our paper were obtained from DAMIT. The exact links to the corresponding asteroids are:

(i) (90265) 2003 CL5 – https://astro.troja.mff.cuni.cz/projects/damit/asteroids/view/1013
(ii) (54827) 2001 NQ8 – https://astro.troja.mff.cuni.cz/projects/damit/asteroids/view/1041
(iii) (60744) 2000 GB93 – https://astro.troja.mff.cuni.cz/projects/damit/asteroids/view/1729
(iv) (56232) 1999 JM31 – https://astro.troja.mff.cuni.cz/projects/damit/asteroids/view/1739

REFERENCES

Allworth J., Windrim L., Bennett J., Bryson M., 2021, Acta Astron., 181, 301
Bartczak P., Dudziński G., 2018, MNRAS, 473, 5050
Bartczak P., Dudziński G., 2019, MNRAS, 485, 2431
Boyd S., Boyd S. P., Vandenberghe L., 2004, Convex Optimization. Cambridge Univ. Press, Cambridge
Carbognani A., Tanga P., Cellino A., Delbo M., Mottola S., Marchese E., 2012, Planet. Space Sci., 73, 80
Dantzig G. B., 1990, in Nash S., ed., A History of Scientific Computing. Addison-Wesley Publishing Company, Boston, MA, p. 141
Ďurech J., Sidorin V., Kaasalainen M., 2010, A&A, 513, A46
Ďurech J. et al., 2011, Icarus, 214, 652
Ďurech J., Hanuš J., Ali-Lagoa V., 2018, A&A, 617, A57
El Ghaoui L., Lebret H., 1997, SIAM J. Matrix Anal. Appl., 18, 1035
Fan S., Frueh C., 2020, J. Astronaut. Sci., 67, 740
Fan S., Friedman A., Frueh C., 2019, in Advanced Maui Optical and Space Surveillance Technologies Conference. Maui Economic Development Board, Maui, HI, p. 23
Friedman A. M., Frueh C., 2018, Acta Astron., 144, 405
Hanuš J. et al., 2011, A&A, 530, A134
Hanuš J., Marchis F., Ďurech J., 2013, Icarus, 226, 1045
Hartley R. I., Kahl F., 2009, Int. J. Comput. Vision, 82, 64
Herrera J. F., Salmerón J. M., Hendrix E. M., Asenjo R., Casado L. G., 2017, J. Global Optim., 69, 547
Horn B. K. P., 1984, Proc. IEEE, 72, 1671
Horst R., Tuy H., 2013, Global Optimization: Deterministic Approaches. Springer Science & Business Media, Berlin
Kaasalainen M., Lamberg L., 2006, Inverse Probl., 22, 749
Kaasalainen M., Torppa J., 2001, Icarus, 153, 24
Kaasalainen M., Lamberg L., Lumme K., Bowell E., 1992a, A&A, 259, 318
Kaasalainen M., Lamberg L., Lumme K., 1992b, A&A, 259, 333
Kaasalainen M., Torppa J., Muinonen K., 2001, Icarus, 153, 37
Li H., Chen W., Zhao J., Bazin J.-C., Luo L., Liu Z., Liu Y.-H., 2020, in 2020 IEEE International Conference on Robotics and Automation (ICRA). IEEE, Paris, p. 2675
Linares R., Furfaro R., Reddy V., 2020, J. Astronaut. Sci., 67, 1063
Little J. J., 1983, in Proceedings of the Third AAAI Conference on Artificial Intelligence. Assoc. Adv. Artif. Intell., Honolulu, p. 247
Liu D., Parra A., Chin T.-J., 2020, in Proceedings of the IEEE/CVF Conference on Computer Vision and Pattern Recognition. IEEE, Seattle, WA, p. 6349
Lumme K., Karttunen H., Bowell E., 1990, A&A, 229, 228
Monteiro F., Silva J. S., Tamayo F., Rodrigues T., Lazzaro D., 2020, MNRAS, 495, 3990
Muinonen K., Lumme K., 2015, A&A, 584, A23
Muinonen K., Wilkman O., Cellino A., Wang X., Wang Y., 2015, Planet. Space Sci., 118, 227
Muinonen K., Torppa J., Wang X.-B., Cellino A., Penttilä A., 2020, A&A, 642, A138
Nocedal J., Wright S., 2006, Numerical Optimization. Springer Science & Business Media, Berlin
Parra Bustos A., Chin T., Eriksson A., Li H., Suter D., 2016, IEEE Trans. Pattern Anal. Mach. Intell., 38, 2227
Pravec P. et al., 2019, Icarus, 333, 429
Press W. H., Teukolsky S. A., Vetterling W. T., Flannery B. P., 1996, Numerical Recipes in Fortran 90: Numerical recipes in Fortran 77V. 2. Numerical recipes in Fortran 90. Cambridge Univ. Press, Cambridge
Rożek A. et al., 2019, A&A, 631, A149
Russell H., 1906, ApJ, 24, 1
Tanga P. et al., 2015, MNRAS, 448, 3382
Viikinkoski M., Kaasalainen M., Ďurech J., 2015, A&A, 576, A8
Vokrouhlický D. et al., 2017a, AJ, 153, 270
Vokrouhlický D. et al., 2017b, A&A, 598, A91
Wang X. et al., 2015, A&A, 581, A55
Yang J., Li H., Campbell D., Jia Y., 2015, IEEE Trans. Pattern Anal. Mach. Intell., 38, 2241

SUPPORTING INFORMATION

Supplementary data are available at *MNRAS* online.

Appendix A. Representation of an object's curvature function with spherical harmonics series.
Appendix B. Derivation of the angular distance in terms of Euler angles.
Appendix C. Experimental results.

Please note: Oxford University Press is not responsible for the content or functionality of any supporting materials supplied by the authors. Any queries (other than missing material) should be directed to the corresponding author for the article.

This paper has been typeset from a TEX/LATEX file prepared by the author.